This document was prepared for the ETI by third parties under contract to the ETI. The ETI is making these documents and data available to the public to inform the debate on low carbon energy innovation and deployment.

Programme Area: Marine

Project: PerAWAT

Title: Report on the Inclusion of FDC Tidal Arrays into DG-ADCIRC Model

Abstract:

WG3 WP6 D5 aims to present the methodology used to describe the fundamental device concept (FDC) tidal arrays in numerical models created for the M2 tidal constituent. The report first introduces the two-dimensional Shallow Water Equations (SWEs) and the chosen numerical method (discontinuous Galerkin finite element method) used to solve these equations. The methodology is then explained for coupling Linear Momentum Actuator Disc Theory (LMADT) to the two-dimensional hydrodynamic model DG-ADCIRC by means of including a line sink of momentum within the discontinuous Galerkin scheme. The verification of the algorithm is undertaken for a number of problems where an array of tidal devices is located in an idealised channel, with different configurations and problem settings. Lastly, preliminary results are given for the Anglesey Skerries, using the modified DGADCIRC code that uses LMADT to calculate the relevant line sink of momentum in the solution domain.

Context:

The Performance Assessment of Wave and Tidal Array Systems (PerAWaT) project, launched in October 2009 with £8m of ETI investment. The project delivered validated, commercial software tools capable of significantly reducing the levels of uncertainty associated with predicting the energy yield of major wave and tidal stream energy arrays. It also produced information that will help reduce commercial risk of future large scale wave and tidal array developments.

Energy Technologies Institute

PerAWaT

WG3 WP6 D5 — REPORT ON THE INCLUSION OF FDC TIDAL ARRAYS INTO DG-ADCIRC MODEL

Authors S. Serhadlioglu, T.A.A. Adcock,
G.T. Houlsby, and A.G.L. Borthwick

Version 2.0

Date 30/7/2012

Revision History		
Issue / Version	Issue Date	Summary
0.1	26/7/2012	Sent to GH for comments
1.0	27/7/2012	Sent to GH
2.0	30/7/2012	Sent to GH

Executive Summary

WG3 WP6 D5 aims to present the methodology used to describe the fundamental device concept (FDC) tidal arrays in numerical models created for the M_2 tidal constituent. The report first introduces the two-dimensional Shallow Water Equations (SWEs) and the chosen numerical method (discontinuous Galerkin finite element method) used to solve these equations. The methodology is then explained for coupling Linear Momentum Actuator Disc Theory (LMADT) to the two-dimensional hydrodynamic model DG-ADCIRC by means of including a line sink of momentum within the discontinuous Galerkin scheme. The verification of the algorithm is undertaken for a number of problems where an array of tidal devices is located in an idealised channel, with different configurations and problem settings. Lastly, preliminary results are given for the Anglesey Skerries, using the modified DG-ADCIRC code that uses LMADT to calculate the relevant line sink of momentum in the solution domain.

Contents

Executive Summary 2

Contents 3

1. Introduction 4

Acceptance Criteria 4

2. Governing Equations 5

3. Discontinuous Galerkin Method 6

HLLC Flux 9

Basis Function 11

Runge-Kutta Time Discretisation 12

4. Representing Tidal Devices in Numerical Models 13

Linear Momentum Actuator Disc Theory (LMADT) 15

Line Sink of Momentum in 2D Hydrodynamic Model DG-ADCIRC 18

Verification Test Cases 21

a. Turbine fence across the width of the channel 22

b. An idealised channel with partial blockage 24

c. Partially blocked channels with complex flow conditions 26

5. Application of Line Sink of Momentum in 2D Depth-Averaged Shallow Water Models 30

Change in M_2 Tidal Constituent in the Anglesey Skerries 32

Power Generation 39

6. Conclusions 40

7. Appendix 40

REFERENCES 45

1. Introduction

Acceptance Criteria

Table 1 lists the acceptance criteria for the present deliverable.

Deliverable	Acceptance criteria	Location in report
WG3 WP6 D5: Report on inclusion of FDC tidal arrays into the numerical models developed in WG3 WP6 M2.	Report describes the methodology used to incorporate tidal arrays into the 2D numerical model, including all algorithms and assumptions.	- Numerical approach: pp: 4-12, - Methodology for including tidal arrays: pp: 13-29, - Application to 2D shallow water model of candidate site: pp: 30 – 40.

Table 1 Acceptance criteria

The report gives a detailed description of the discontinuous Galerkin method, which has been selected for solving the 2D shallow water equations (SWEs). A brief summary of the methodologies for including the effects of tidal devices in two-dimensional hydrodynamic models is given herein. Section 4 explains linear momentum actuator disc theory (LMADT), which is used to represent the tidal devices in the hydrodynamic model. Section 5 provides example application of the line sink of momentum algorithm to turbine fences located in the Anglesey Skerries. Section 6 provides the conclusions. Section 7 introduces the preliminary results for the Pentland Firth model using enhanced bed friction methodology.

2. Governing Equations

The ocean tides are modelled using the long wave equations, commonly known as the shallow water equations (SWEs). The flow is assumed to be nearly horizontal, thus the acceleration of the particles in the vertical direction is negligible (see *e.g.*, Falconer, 1993). By defining the system as nearly horizontal, the pressure distribution in the vertical direction is assumed hydrostatic (see *e.g.*, Falconer, 1993). The established governing equations can be expressed as a time dependent, two-dimensional system of non-linear partial differential equations of hyperbolic type (Toro, 2001), which can be shown as,

$$\frac{\partial \zeta}{\partial t} + \frac{\partial}{\partial x}\left(Hu\right) + \frac{\partial}{\partial y}\left(Hv\right) = 0, \qquad 2.1$$

$$\frac{\partial}{\partial t}\left(uH\right) + \frac{\partial}{\partial x}\left(Hu^2 + \frac{1}{2}g\left(H^2 - h^2\right)\right) + \frac{\partial}{\partial y}\left(Huv\right) = g\zeta\frac{\partial h}{\partial x} - \tau uH + fv + F_x, \qquad 2.2$$

$$\frac{\partial}{\partial t}\left(vH\right) + \frac{\partial}{\partial x}\left(Huv\right) + \frac{\partial}{\partial y}\left(Hv^2 + \frac{1}{2}g\left(H^2 - h^2\right)\right) = g\zeta\frac{\partial h}{\partial y} - \tau vH - fu + F_y. \qquad 2.3$$

Equation 2.1 is the mass conservation equation, where ζ represents the water elevation above a certain datum, H is the total depth of the water column ($H = \zeta + h$), which is equivalent to the sum of free surface elevation (ζ) and the bathymetric depth of the water column below the geoid (h). The variables u and v represent the depth-averaged velocities in x- and y- directions. Equation 2.2 and Equation 2.3 are the momentum conservation equations in x- and y- directions respectively, where g is the gravitational acceleration, τ is the bottom friction factor, f is the Coriolis force, and F_x and F_y represent additional forces in the system such as tidal potential forces, wind or wave radiation stresses, *etc*.

The above equations can be rewritten in divergence form as shown in Equation 2.4,

$$\frac{\partial \mathbf{u}}{\partial t} + \nabla\cdot\mathbf{F}\left(\mathbf{u}\right) = \mathbf{s}\left(\mathbf{u}\right), \qquad 2.4$$

where $\mathbf{u}$ is vector of conserved variables,

$$\mathbf{u} = \left[\zeta, uH, vH\right]^T, \tag{2.5}$$

F is the flux vector,

$$\mathbf{F} = \left[\mathbf{f}_x, \mathbf{f}_y\right] = \begin{bmatrix} uH & vH \\ Hu^2 + \frac{1}{2}g\left(H^2 - h^2\right) & Huv \\ Huv & Hv^2 + \frac{1}{2}g\left(H^2 - h^2\right) \end{bmatrix} \tag{2.6}$$

and **s** is the source (or sink) term vector,

$$\mathbf{s} = \left[0, g\zeta\frac{\partial h}{\partial x} - \tau uH + fv + F_x, g\zeta\frac{\partial h}{\partial y} - \tau vH - fu + F_x\right]^T. \tag{2.7}$$

In this form, it is seen that the two-dimensional flux vector defines the transport of $\mathbf{u}\left(\mathbf{x}, t\right)$. In order to solve the equation system, appropriate initial and boundary conditions must also be supplied. Section 3 describes the discontinuous Galerkin method, which is used to solve the SWEs numerically.

3. Discontinuous Galerkin Method

Numerical solutions to the hyperbolic shallow water equations have been obtained over the years using different numerical schemes (see *e.g.* Abbott, 1978; Vreugdenhil, 1994; Wei Yan, 1992). Selection of the numerical scheme is of importance, and in particular affects the necessary level of discretization, which in turn affects the accuracy of the solution obtained (Garcia-Navarro *et al.*, 2008). In the literature, the most commonly used numerical schemes for solving the SWEs are the finite difference method (FD), finite element methods (FE), and finite volume method (FV). In WG3 WP6, the discontinuous Galerkin (DG) method has been chosen in order to solve the SWEs. It is a method, which has characteristics of both FE and FV methods (Cockburn and Shu, 1998). While naturally inheriting some features from these methods, (*e.g.*, compatibility with unstructured triangular and/or quadrilateral elements, or application of boundary conditions through the use of numerical fluxes [Draper, 2011; Ferrer, 2012]), the main advantage of using the DG method is its

ability to conserve mass locally (Blain and Massey, 2005). This is achieved, as the DG formulation imposes the weak formulation of the governing equations individually for each element. Draper (2011) discusses that conserving mass flux is of importance in order to represent the relevant momentum sink that occurs with respect to the existence of tidal devices in the area being modelled. Introducing a discontinuity in the solution, such as a line sink of momentum, is also easy to implement in a piece-wise method such as the DG method.

Following the discussions above, the first step in space discretisation by the DG method is to divide the flow domain, Ω into N_e number of non-overlapping but not necessarily conforming elements, e each with an elemental domain of Ω_e and elemental boundary of $\partial\Omega_e$,

$$\Omega = \bigcup_{e=1}^{N_e} \Omega_e. \tag{3.1}$$

Following the standard Galerkin method, a weak formulation of the governing equation is required. Multiplying Equation 2.4 with a test function $\phi_h \in V_h$ and integrating over each element we obtain,

$$\left(\frac{\partial \mathbf{u}}{\partial t}, \phi_h\right)_{\Omega_e} + \left(\nabla \cdot \mathbf{F}(\mathbf{u}), \phi_h\right)_{\Omega_e} = \left(\mathbf{s}(\mathbf{u}), \phi_h\right)_{\Omega_e}. \tag{3.2}$$

The test function ϕ_h belongs to V_h which is a discrete space of piecewise functions that are differentiable over an element, while allowing discontinuities at element boundaries,

$$V_h = \left\{\phi_h \in L^2(\Omega) : \phi_h \middle| \Omega_e \in P^k(\Omega_e), \forall \Omega_e\right\}. \tag{3.3}$$

In Equation 3.3, $P^k(\Omega_e)$ indicates the space of polynomials of order k for elements with linear elemental mappings. The next step in writing the weak DG formulation is to substitute the exact solution $\boldsymbol{u}$ by an approximate solution $\boldsymbol{u}_h$. Applying the divergence theorem (Gauss' theorem) to the advection term of the equation obtained, Equation 3.2 becomes,

$$\left(\frac{\partial \mathbf{u}_h}{\partial t},\phi_h\right)_{\Omega_e} - \left(\nabla\phi_h,\mathbf{F}\left(\mathbf{u}_h\right)\right)_{\Omega_e} + \left\langle \mathbf{F}\left(\mathbf{u}_h^-\right)\cdot\mathbf{n},\phi_h^-\right\rangle_{\partial\Omega_e} - \left(\mathbf{s}\left(\mathbf{u}_h\right),\phi_h\right)_{\Omega_e} = 0. \qquad 3.4$$

In Equation 3.4, $\mathbf{n} = \left[n_x, n_y\right]^T$ is the outward normal vector to the element boundary $\partial\Omega_e$, and the terms $\mathbf{u}_h^-$ and ϕ_h^- are the *traces* of $\mathbf{u}_h$ and ϕ_h respectively (Houston *et al.*, 2002; Tassi *et al.*, 2007). The trace terms are associated with the discontinuity along the elemental boundaries, where dual values for discrete solution $\mathbf{u}_h$ and the flux $\mathbf{F}\left(\mathbf{u}_h\right)$ are possible while the functions defined within V_h are continuous on the interior of each element (Karniadakis and Sherwin, 2005). Equation 3.4 can be solved by replacing the flux term on the boundary by a numerical flux of choice $\hat{\mathbf{F}}\left(\mathbf{u}_h^{int},\mathbf{u}_h^{ext}\right)$, which depends on the trace values of the discrete solution $\mathbf{u}_h$ on the interior $\left(\mathbf{u}_h^{int}\right)$ and exterior $\left(\mathbf{u}_h^{ext}\right)$ of the element (Figure 1). Substituting the numerical flux in Equation 3.4 gives,

$$\left(\frac{\partial \mathbf{u}_h}{\partial t},\phi_h\right)_{\Omega_e} - \left(\nabla\phi_h,\mathbf{F}\left(\mathbf{u}_h\right)\right)_{\Omega_e} + \left\langle \hat{\mathbf{F}}\left(\mathbf{u}_h^{int},\mathbf{u}_h^{ext}\right)\cdot\mathbf{n},\phi_h^-\right\rangle_{\partial\Omega_e} - \left(\mathbf{s}\left(\mathbf{u}_h\right),\phi_h\right)_{\Omega_e} = 0. \qquad 3.5$$

Equation 3.5 shows that the boundary flux is normal to the element edges, which means that a local Riemann problem can be solved for the given interior $\left(\mathbf{u}_h^{int}\right)$ and exterior fluxes $\left(\mathbf{u}_h^{ext}\right)$.

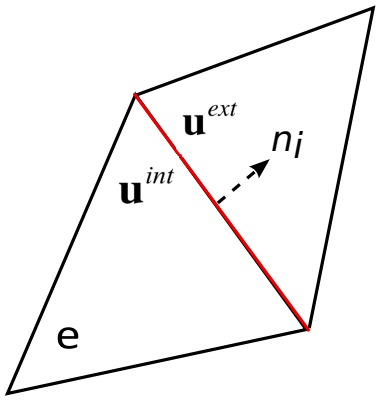

Figure 1 Representation of a pair of neighbouring elements. The element *e* has a common edge *i* (shown as red line), where n_i is the normal to the edge, u^{int} is the solution on the egde *i* when

approaching from inside of element e and u^{ext} is the solution on the edge i when approaching from external to the edge (Kubatko *et al*., 2006).

Any upwinding numerical flux method can be used in Equation 3.5. In the DG literature, the most commonly used numerical fluxes are: Roe's average flux, Lax-Friedrich flux, and HLL/HLLC flux. The verification test cases presented in this report utilise HLLC for its stability and efficiency.

HLLC Flux

Rewriting the numerical flux term given in Equation 3.5 using the elemental inner product expansion $\left\langle a,\mathbf{b}\right\rangle_{\partial\Omega_e} \equiv \int_{\partial\Omega_e} a\mathbf{b}\cdot\mathbf{n}d\Gamma$, we obtain,

$$\sum_{\ell}^{\Gamma}\left\{\int_{\ell}\left(\phi_h^{int}-\phi_h^{ext}\right)\hat{\mathbf{F}}\left(\mathbf{u}_h^{int},\mathbf{u}_h^{ext}\right)\cdot\mathbf{n}d\Gamma\right\} \qquad 3.6$$

where a single edge on an element is denoted as ℓ and the set of all edges in the flow domain (including the domain boundary) is $\Gamma\equiv\Omega\cup\partial\Omega$. The set of interior edges is denoted as Γ^{int} and the exterior edges where the boundary conditions are applied is given as $\Gamma^{ext}\equiv\Gamma^{bc}$. Since the numerical flux $\hat{\mathbf{F}}\left(\mathbf{u}_h^{int},\mathbf{u}_h^{ext}\right)$ is normal to the elemental boundary edge, a one-dimensional local Riemann problem can be solved for the fluxes when the trace values $\mathbf{u}_h^{int}$ and $\mathbf{u}_h^{ext}$ are imposed. The trace value of $\mathbf{u}_h^{ext}$ is dependent on the boundary condition $\mathbf{u}_h^{ext}=\mathbf{u}^{bc}$, which is applied at edges that belong to the flow domain, $\ell\in\Gamma^{bc}$. Considering that the flux is conservative, an approximation to $\mathbf{u}_h^{int}$ can be obtained. In the conventional HLL method, the relations provided above are used to estimate wave speeds at the interior (s^{int}) and exterior (s^{ext}) of the edge (Toro, 2001). The HLLC method requires estimation of an additional contact wave speed (s^{*}) such that,

$$
\begin{aligned}
s^{int} &= \overline{u}^{int} - \sqrt{gH^{int}}\,q^{int}, \\
s^{ext} &= \overline{u}^{ext} + \sqrt{gH^{ext}}\,q^{ext}, \\
s^{*} &= \frac{s^{int}H^{ext}\left(\overline{u}^{ext} - \overline{u}^{int}\right) - s^{ext}H^{int}\left(\overline{u}^{int} - s^{int}\right)}{H^{ext}\left(\overline{u}^{ext} - s^{ext}\right) - H^{int}\left(\overline{u}^{int} - s^{int}\right)}
\end{aligned}
\qquad 3.7
$$

where,

$$
q^{(int,ext)} = \begin{cases} \sqrt{\left(H^{*}\right)^{2} + H^{*}H^{(int,ext)} \Big/ 2\left(H^{(int,ext)}\right)^{2}} & if\ H^{*} > H^{(int,ext)} \\ 1 & if\ H^{*} \le H^{(int,ext)} \end{cases}. \qquad 3.8
$$

In Equation 3.7 $\overline{u}$ is the velocity normal to the edge, $c = \sqrt{gH}$ is the celerity of a gravity wave, H is the total water depth, and q is the correction factor. The estimated wave speed for the contact wave s^{*} is equivalent to $\overline{u}^{*}$ in exact Riemann solvers (Toro, 2001). In the computation of the correction factor (Equation 3.8), the water depth on the contact wave is calculated assuming that the interior and exterior (left and right) waves are rarefaction waves (Toro, 2001),

$$
H^{*} = \frac{1}{g}\left(\frac{1}{2}\left(\sqrt{gH^{int}} + \sqrt{gH^{ext}}\right) + \frac{1}{4}\left(\overline{u}^{int} - \overline{u}^{ext}\right)\right)^{2}. \qquad 3.9
$$

After the wave speeds are estimated, the HLLC flux can be expressed as,

$$
\mathbf{F}^{HLLC} = \begin{cases} \mathbf{F}^{int} & s^{int} < 0, \\ \mathbf{F}_{*}^{int} & s^{int} \le 0 < s^{*}, \\ \mathbf{F}_{*}^{ext} & s^{*} \le 0 \le s^{ext}, \\ \mathbf{F}^{ext} & s^{ext} < 0, \end{cases} \qquad 3.10
$$

where,

$$
\begin{aligned}
\mathbf{F}_{*}^{int} &= \mathbf{F}^{int} + s^{int}\left(\mathbf{u}_{*}^{int} - \mathbf{u}^{int}\right), \\
\mathbf{F}_{*}^{ext} &= \mathbf{F}^{ext} + s^{ext}\left(\mathbf{u}_{*}^{ext} - \mathbf{u}^{ext}\right).
\end{aligned}
\qquad 3.11
$$

Equation 3.11 is used to calculate the fluxes related to the contact wave. The fluxes on the interior and exterior of the edge are given as $\mathbf{F}^{int} = \mathbf{F}\left(\mathbf{u}^{int}\right)$ and $\mathbf{F}^{ext} = \mathbf{F}\left(\mathbf{u}^{ext}\right)$, and the states $\mathbf{u}_*^{int}$ and $\mathbf{u}_*^{ext}$ are obtained by,

$$\mathbf{u}_*^{(int,ext)} = H^{(int,ext)}\left(\frac{s^{(int,ext)} - \overline{u}^{(int,ext)}}{s^{(int,ext)} - s^*}\right)\begin{bmatrix} 1 \\ s^* \\ \overline{v}^{(int,ext)} \end{bmatrix}. \qquad 3.12$$

Basis Function

Cockburn and Shu (1998) explain that a suitable basis function with sufficient degrees of freedom may simplify the implementation of the DG method while improving the computational efficiency. By using the hierarchical and orthogonal basis function proposed by Dubiner (1998), high-order elements are constructed by means of adding terms to the lower-order elements (Kubatko *et al.*, 2006). The basis function is obtained as a product of polynomials, which can be given as (Karniadakis and Sherwin, 2005),

$$\phi_{pq}\left(\xi_1, \xi_2\right) = P_p^{0,0}\left(\eta_1\right)\left(\frac{1-\eta_2}{2}\right)^p P_q^{2p+1,0}\left(\eta_2\right) \qquad 3.13$$

In Equation 3.13, $P_K^{\alpha,\beta}$ defines the K^{th} order Jacobi polynomial of weights α and β. ξ_1 and ξ_2 correspond to the coordinates of the master triangle shown in Figure 2 and η_1 and η_2 are the coordinates of the corresponding mapped quadrilateral element in Figure 2.

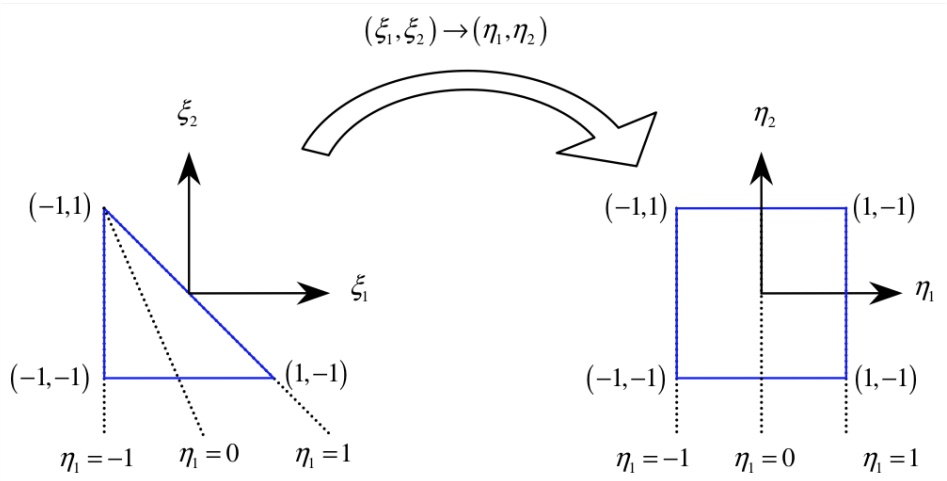

Figure 2 Mapping of the master triangle in collapsed coordinates (Kubatko *et al.*, 2006).

This mapping can be formulated as (see *e.g.* Kubatko *et al.*, 2006),

$$\eta_1 = 2\frac{(1+\xi_1)}{(1-\xi_2)} - 1, \quad \eta_2 = \xi_2 \tag{3.14}$$

Using Equation 3.14, the approximate solution can be rewritten as,

$$\mathbf{u}_h = \sum_p \sum_q \tilde{\mathbf{u}}_{pq}\, \phi_{pq}. \tag{3.15}$$

In Equation 3.15, the modal degrees of freedom are represented by $\tilde{\mathbf{u}}_{pq}$, and, the trial (test) functions ϕ_{pq} are given by Equation 3.13.

Runge-Kutta Time Discretisation

Application of the discontinuous Galerkin method to space discretization reduces the system of hyperbolic partial differential equations to one of ordinary differential equations, which can be given as,

$$\frac{\partial \mathbf{u}_h}{\partial t} = \mathbf{L}_h(\mathbf{u}_h). \tag{3.16}$$

In order to discretize these ordinary differential equations in time, the total variation diminishing Runge-Kutta scheme (Shu and Osher, 1988) is utilized. For high order

spatial approximations where $p > 1$, a high-order TVD Runge-Kutta scheme can be given as Equation 3.17 for time increment *n* to *n+1*,

$$\begin{aligned}
\mathbf{u}_h^{\mathbf{1}} &= \mathbf{u}_h^{\mathbf{n}} + \Delta t \mathbf{L}_h\left(\mathbf{u}_h^{\mathbf{n}}\right) \\
\mathbf{u}_h^{\mathbf{2}} &= \frac{3}{4}\mathbf{u}_h^{\mathbf{n}} + \frac{1}{4}\left(\mathbf{u}_h^{\mathbf{1}} + \Delta t \mathbf{L}_h\left(\mathbf{u}_h^{\mathbf{1}}\right)\right) \\
\mathbf{u}_h^{\mathbf{n+1}} &= \frac{1}{3}\mathbf{u}_h^{\mathbf{n}} + \frac{2}{3}\left(\mathbf{u}_h^{\mathbf{2}} + \Delta t \mathbf{L}_h\left(\mathbf{u}_h^{\mathbf{2}}\right)\right)
\end{aligned} \qquad 3.17$$

Because of the explicit nature of the scheme, a limitation on the time step is necessary, which is defined by the Courant-Friedrichs-Lewy (CFL) condition (Kubatko *et al.*, 2006),

$$\Delta t \le min_{\Omega_e}\left(\frac{h_e}{\left|\lambda_{max}\right|_e\left(2p+1\right)}\right) \qquad 3.18$$

where h_e is diameter of the element *e* and λ_{max} is the estimated maximum eigenvalue, *p* is the polynomial degrees, and Δt is the time step.

4. Representing Tidal Devices in Numerical Models

The inclusion of tidal turbines into a depth-averaged flow is always going to require simplification of the real physics, and cannot correctly model the flow local to the turbines. This is because the depth-averaged models cannot account for complicated vertical velocity profiles and has a length scale which is greater than the water depth. The flow through a tidal turbine will have a complicated vertical profile and variations with length scales much less than the water depth. Our objective is therefore to ensure that the correct momentum and energy are extracted from the overall flow, but not to attempt to model the details of the wake as this is beyond the scope of our model, and attempting to do so will only produce effects that are unphysical.

There are two methods that have been considered for extracting energy from the flow. Either the turbines can be represented as a discontinuity in the flow (e.g. Draper *et al.*, 2010) or the drag can be smeared over an area by enhancing the bed friction of a

given node (e.g. Sutherland *et al.*, 2007). One of the objectives of this project is to compare the two methodologies.

Representing turbines as a discontinuity in the flow requires that the difference in water level across a tidal turbine to be known as a function of relevant parameters characterising the turbines and flow. In this approach it is assumed that the length of which the wake mixes (and thus a downstream water depth is fixed) is small in comparison to an element. The parameter used in the enhanced bed friction method is the turbines thrust coefficient. The parameters used to define these models are mutually dependent, and if the head loss is known then an effective thrust coefficient may be calculated and *vice versa*.

It is as yet unclear which is the "better" approach for representing turbines. Using a discontinuity has the advantage that the size of the surrounding elements should not affect the solution, and also generally means that a coarser resolution may be used (with consequent numerical advantages). However, for pragmatic reasons enhancing bed friction may be preferable as it requires less (or even no) changes to the source code and is expected to give results very close to the alternative. Subsequent deliverables will compare the results of the different methodologies. However, it is unlikely to determine which gives a more accurate representation of turbines in a depth-averaged flow, as there is no data available to for comparison.

Including enhanced bed friction in the model is straightforward, and has already been shown to produce the correct power output in WG3 WP6 D3. In the appendix to this deliverable preliminary results are presented by applying the enhanced bed friction methodology to the Pentland Firth region.

The bulk of this deliverable considers the implementation and verification of the line discontinuity method into DG-ADCIRC. In this deliverable, where applicable we use actuator disc theory (described in detail in the next section) to model the presence of

turbines in the flow. It is straightforward to extend this to other parameterisations of the flow through a tidal turbine.

Linear Momentum Actuator Disc Theory (LMADT)

LMADT is an extension to actuator disc theory (ADT), which was first proposed by Froude (1889) to represent the local steady flow field generated by a ship propeller. The theory was then applied by Lanchester (1915) and Betz (1920) independently to assess the performance of wind turbines (Van Kuik, 2007). In their studies, Lanchester and Betz show that the power available to the turbine cannot exceed 16/27 of the total upstream kinetic energy flux passing through the actuator disc. This upper limit is called the Lanchester-Betz limit, and it has been used to design wind turbines over many years. The successful utilization of wind as a renewable energy source has encouraged engineers to start applying LMADT to the analogous design of tidal turbines. However, standard LMADT assumes unbounded flow conditions, and hence is not applicable to tidal turbine design in a straightforward way. Bryden *et al.* (2007) emphasise that the standard Betz model is derived assuming that the flow is incompressible and unconstrained, meaning that the boundaries are sufficiently far away from the turbines. On the other hand, in open channel flow, the flow is constrained by the seabed and the free surface, which influences the behaviour of the downstream flow. Furthermore, the operating fluid (water) must be treated as heavy, as there are important gravitational effects, which do not feature in the original analysis. The derivation of LMADT applied on an open channel has been given by Houlsby *et al.* (2008) and Draper (2011) and hence will not be repeated herein. In WG3 WP6 D5, it is aimed to introduce the important results obtained from LMADT derivation for open channel flows that are applied in the numerical model DG-ADCIRC.

The flow field is indicated as in Figure 3 for an open channel flow with a free surface elevation. The flow field is divided into several stations for the analysis. Assuming that the pressure is hydrostatic and the flow is uniform at stations 1,4 and 5, and the bypass flow is uniform, it is possible to write the bypass flow $u_{b4} = \beta_4 u$ at Station 4 (Houlsby *et al.*, 2008). The turbine flow velocities at stations 2 and 4 are given as $u_{t2} = \alpha_2 u$ and $u_{t4} = \alpha_4 u$ respectively. In Figure 3, T represents the thrust applied to

the flow by the turbine with an area of *A,* and a blockage ratio of $B = A/hb$. In the figure, *X* indicates a constraining force between the turbine streamtube and the bypass flow (Houlsby *et al.*, 2008).

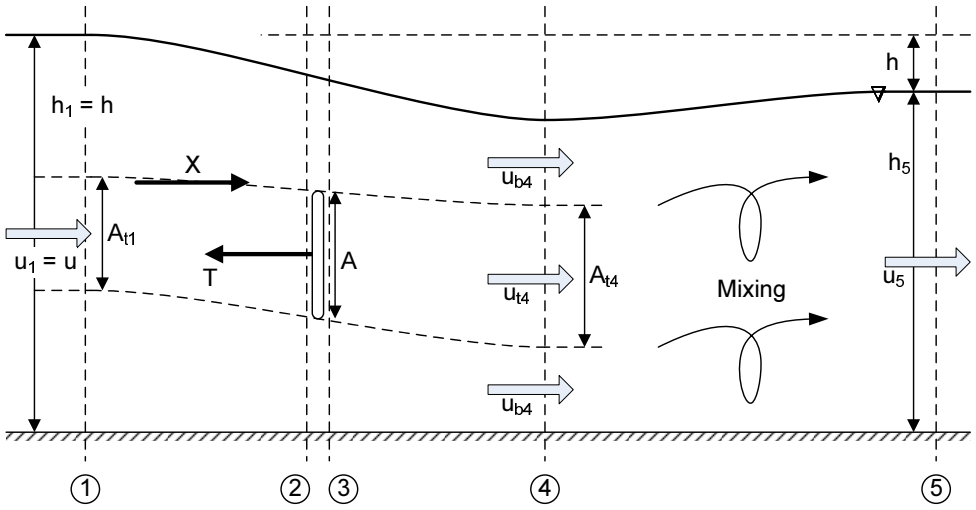

Figure 3 An actuator disc placed in an open channel flow with a free water surface (figure taken from Houlsby *et al.*, 2008)

Following the derivation conducted by Houlsby *et al.* (2008), the constant pressure-volume boundary derivation of the LMADT gives,

$$\alpha_2 = \frac{2\left(\beta_4 + \alpha_4\right) - \dfrac{\left(\beta_4 - 1\right)^3}{B\beta_4\left(\beta_4 - \alpha_4\right)}}{4 + \dfrac{\left(\beta_4^2 - 1\right)}{\alpha_4\beta_4}} \qquad 4.1$$

where *B* is the blockage ratio, α_4 is the wake velocity coefficient, β_4 is the bypass flow velocity coefficient and, α_2 is the turbine flow velocity coefficient. Equation 4.1 provides a relation between the upstream and downstream flow velocities which accounts for the effect of the bypass flow and can be solved once *B* and β_4 are prescribed, while defining either α_2 or α_4. Solution of Equation 4.1 is of importance for calculating the thrust applied and power extracted by the turbine. Considering that

the bypass flow velocity coefficient will change with respect to the variable upstream Froude number, β_4 can be calculated from,

$$\frac{Fr^2}{2}\beta_4^4 + 2\alpha_4 Fr^2\beta_4^3 - \left(2 - 2B + Fr^2\right)\beta_4^2 - \left(4\alpha_4 + 2\alpha_4 Fr^2 - 4\right)\beta_4 + \left(\frac{Fr^2}{2} + 4\alpha_4 - 2B\alpha_4^2 - 2\right) = 0. \quad 4.2$$

Equation 4.2 is quartic in β_4, and can be solved for defined blockage ratio *B*, upstream Froude number *Fr* and, wake velocity coefficient α_4. The thrust applied by the turbine and the power that is available to the turbine can be given as (Houlsby *et al.*, 2008),

$$T = \frac{1}{2}\rho u^2 BbH\left(\beta_4^2 - \alpha_4^2\right) = \frac{1}{2}\rho u^2 BbHC_T,$$
$$P = \frac{1}{2}\rho u^3 BbH\alpha_2\left(\beta_4^2 - \alpha_4^2\right) = \frac{1}{2}\rho u^3 BbHC_P, \quad 4.3$$

where ρ is the water density, *B* is the blockage ratio, *b* is the width of the channel, *H* is the total water depth in the channel, β_4 is the by-pass flow coefficient and α_4 is the turbine wake induction factor. In Equation 4.3, thrust coefficient is $C_T = \beta_4^2 - \alpha_4^2$ and $C_P = \alpha_2 C_T = \alpha_2\left(\beta_4^2 - \alpha_4^2\right)$. It is important to highlight one important result from the analysis made by Houlsby *et al.* (2008) and Draper (2011), which is that the actuator disc is removing potential energy from the flow rather than the kinetic energy, which can be seen as a relative head difference between the upstream and downstream of the turbine. Considering that the flow will mix when it passes through the turbine, momentum conservation can be applied in the horizontal direction between upstream and downstream of the turbine to show the relative depth change in the flow field,

$$\frac{1}{2}\left(\frac{\Delta H}{H}\right)^3 - \frac{3}{2}\left(\frac{\Delta H}{H}\right)^2 + \left(1 - Fr^2 + \frac{C_T BFr^2}{2}\right)\frac{\Delta H}{H} - \frac{C_T BFr^2}{2} = 0, \quad 4.4$$

where *H* is the total water depth, *Fr* is the upstream Froude number, C_T is the thrust coefficient and, *B* is the blockage ratio. Equation 4.4 is a cubic equation which defines the relative head drop when the characteristics of the turbine are defined. To conserve mass, the head drop downstream of the turbine then leads to an increase in the

velocity. In the next subsection, the introduction of the tidal devices defined by LMADT (Houlsby *et al.*, 2008) into a two-dimensional depth-averaged model will be explained.

Line Sink of Momentum in 2D Hydrodynamic Model DG-ADCIRC

The key advantages of using LMADT are its use of theoretical characteristics to relate tidal devices to the thrust applied to the flow by them, and the distinction between power extracted by the devices to the power available to a tidal fence (Draper, 2011). Following Draper (2011), a fence of tidal devices can be modelled as a line sink of momentum in a two-dimensional depth-averaged shallow water model. In order to achieve this goal, several assumptions need to be made, which can be summarised as follows,

- tidal devices are placed periodically (centre-to-centre) within the fence,
- the thrust applied locally by the turbines will suffice to dominate the bed friction and inertia forces,
- the blockage ratio, channel depth and width are changing slowly with time and,
- the length of the mixing zone is smaller than the size of an element.

Considering the space discretisation of the flow domain using the discontinuous Galerkin method, in addition to the assumptions presented above, it is possible to represent the turbines as an edge of an element in the computational domain. The momentum sink is then computed by modifying the numerical flux that is used to couple the elements. Figure 4 depicts two elements that share a common edge, representing a turbine where a line discontinuity occurs. When approaching the edge from the interior of the element *A*, the primitive variables on a Gauss point along the edge are given as, $H^{in}, \overline{u}^{in}, \overline{v}^{in}$ and when approaching from the exterior, the corresponding variables are $H^{ex}, \overline{u}^{ex}, \overline{v}^{ex}$ [which represent the total water depth ($H = h_b + \zeta$), normal velocity component in the horizontal direction, and the tangential velocity component respectively]. Bearing in mind that the effect of turbines is represented by means of a line sink of momentum in the flow field, the fluxes out of

the element A, $F\left(H_*^{in}, \overline{u}_*^{in}, \overline{v}_*^{in}\right)$ and into the element, $F\left(H_*^{ex}, \overline{u}_*^{ex}, \overline{v}_*^{ex}\right)$ need to be altered to represent the momentum loss.

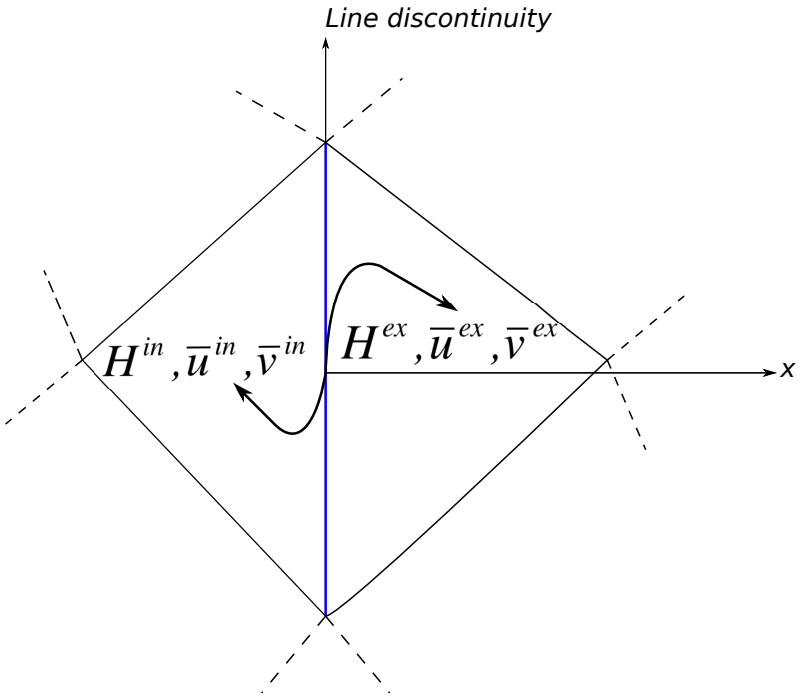

Figure 4 Neighbouring elements with a line discontinuity, shown as the blue line [Figure is based on representation used by Draper (2011)].

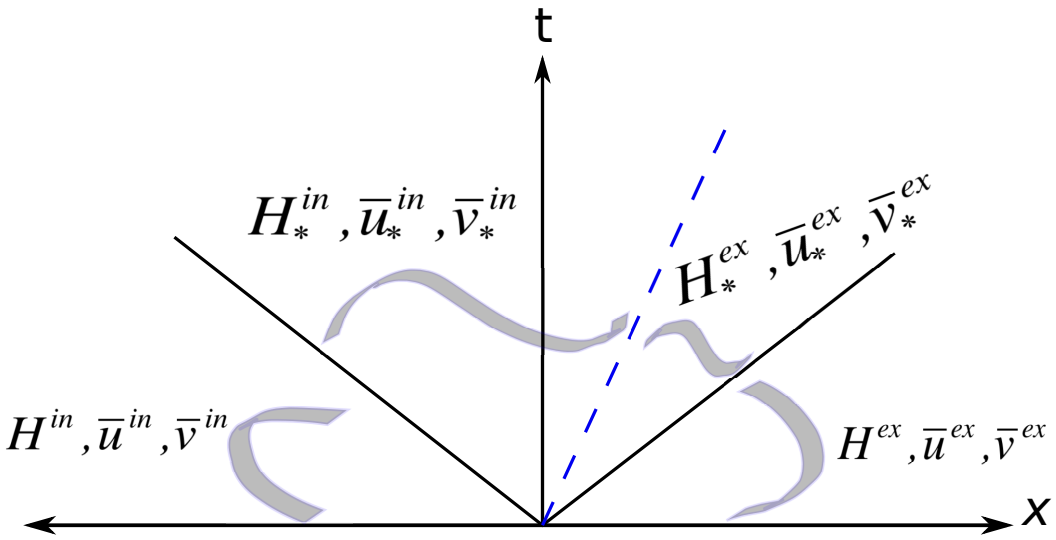

Figure 5 Wave structure on the common edge of the neighbouring elements. The solid black lines are the rarefaction waves coming in and going out of the element; the dashed blue line represents the contact discontinuity (Toro, 2001).

Assuming that the flow remains sub-critical, (which it will do for all the relevant tidal flows), the wave structure on the common edge then can be shown as in Figure 5. The solid lines in Figure 5 represent the shock and rarefaction waves whereas the dashed line is the contact discontinuity occurring due to the existence of the tangential velocity component (Toro, 2001). The interface values $H_*^{in}, \overline{u}_*^{in}, H_*^{ex}, \overline{u}_*^{ex}$ then represent the solution of a one-dimensional local Riemann problem, which would satisfy the conditions,

$$H_*^{in}\overline{u}_*^{in} = H_*^{ex}\overline{u}_*^{ex} \tag{4.5}$$

$$\overline{u}^{in} + 2c^{in} = \overline{u}_*^{in} + 2c_*^{in} \tag{4.6}$$

$$\overline{u}^{ex} - 2c^{ex} = \overline{u}_*^{ex} - 2c_*^{ex} \tag{4.7}$$

Equation 4.5 ensures mass conservation at the edge of the element. Equation 4.6 and Equation 4.7 conserve the Riemann invariants along the characteristic lines normal to the boundary. In order to account for the momentum sink across the turbine edges, one more condition must be assigned. LMADT applied to uniform flow predicts that the turbines will remove potential energy from the flow. Adopting Equation 4.4 to the above set of equations,

$$\frac{1}{2}\left(\frac{\Delta H}{H}\right)^3 - \frac{3}{2}\left(\frac{\Delta H}{H}\right)^2 + \left(1 - Fr^2 + \frac{C_T B Fr^2}{2}\right)\frac{\Delta H}{H} - \frac{C_T B Fr^2}{2} = 0, \tag{4.8}$$

it is then possible to define uniquely the interface values. Equation 4.8 provides a relation for the head drop across the turbine and the upstream head, where $\Delta H^* = \left|H_*^{in} - H_*^{ex}\right|$ is the head difference at the interface, H^* is the total water depth, C_T is the thrust coefficient and Fr is the upstream Froude number. The thrust coefficient is obtained from,

$$C_T = \beta_4^2 - \alpha_4^2 \tag{4.9}$$

where β_4 is the by-pass flow coefficient and α_4 is the turbine wake induction factor. In the present work, the by-pass flow coefficient β_4, is computed by solving the quartic equation (Equation 4.2) using the Newton-Raphson method for a given blockage ratio

(B) and wake induction factor (α_4). The computed thrust coefficient is then substituted into Equation 4.8. Considering that equations 4.5, 4.6 and, 4.7 depend on the primitive variables, the relative depth change in Equation 4.8 is rewritten as,

$$\frac{\Delta H^*}{H^*} = \frac{H_*^{upstream} - H_*^{downstream}}{H_*^{upstream}} = 1 - \frac{H_*^{downstream}}{H_*^{upstream}}. \qquad 4.10$$

Substituting Equation 4.10 into Equation 4.8, we get the depressed cubic expression,

$$x^3 + \left(C_T B Fr^2 - 2Fr^2 - 1\right)x + 2Fr^2 = 0, \qquad 4.11$$

where x is the ratio between downstream ($H^{downstream}$) and upstream ($H^{upstream}$) total water depths. Equation 4.11 is solved for x to obtain the ratio of downstream depth to the upstream. Using the conservation of mass given in Equation 4.5, we can derive the relations between primitive variables follows,

$$\begin{aligned} \overline{u}_*^{downstream} &= \frac{\overline{u}_*^{upstream}}{x}, \\ c_*^{downstream} &= \sqrt{x} c_*^{upstream}. \end{aligned} \qquad 4.12$$

Lastly, the relations in Equation 4.12 are substituted into Equations 4.6 and 4.7 to calculate the altered upstream normal velocity and wave speed. The algorithm used in DG-ADCIRC first considers the direction of the propagation of information, and then the above equations are solved for the primitive variables.

Verification Test Cases

The verification test cases include two general configurations of an idealised fence of tidal devices inserted in an open channel. The first of these configurations considers a narrow channel where a fence is deployed completely across the width of the channel. In this scenario, it is expected that the flow will separate around the area of a turbine and then mix with the flow passing through it, creating a mixing zone downstream on the fence (Draper, 2011). In the second configuration, similar ideal fences are deployed in an unbounded flow. The partially blocked flow case is then extended to different problems, which consider different configurations within the computational domain, in order to test the accuracy and stability of the modified DG-ADCRIC code.

a. Turbine fence across the width of the channel

The test case used for the verification of the algorithm is based on an idealised channel, which is forced by an inflow of constant discharge at the upstream boundary and has a specified water depth at the downstream boundary. The channel width and length are set to 400 m and 1000 m respectively. The depth of the channel is 1 m. In the simulations, there is no bed friction. The turbine fence is located in the middle of the channel, and extends across the entire width of the channel. In order to test the algorithm, various flow rates are selected in order to alter the upstream Froude number. The comparisons are then undertaken against different upstream blockage ratios and wake induction factors to differing upstream Froude numbers, and are undertaken against the analytical solution from LMADT, and the results for different upstream flow conditions. These comparisons are plotted in Figure 7.

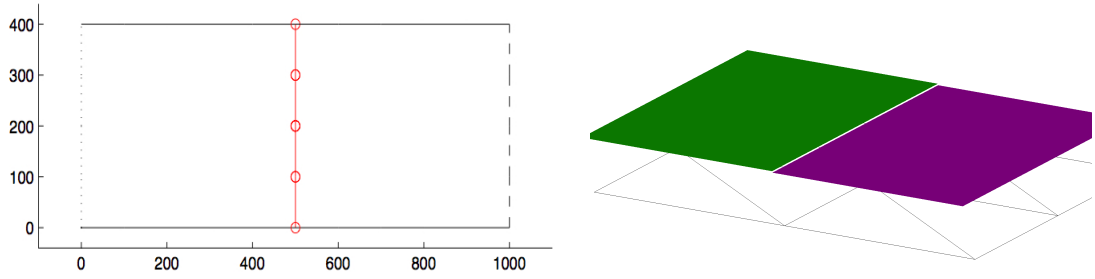

Figure 6 The problem geometry (left- image taken from Draper, 2011). The turbines are located in the middle of the channel across the width of the channel. The channel is forced with a specified flux on the upstream, and on the downstream the elevation is defined. Relative head drop seen in the flow field (right).

The DG-ADCIRC model results are in a very good agreement with the analytical solution. Figure 6 shows the problem geometry (left) and the relative head difference observed on the flow domain (right), which is plotted on top of the computational mesh. Figure 7 presents the comparisons of different blockage ratios for various upstream conditions.

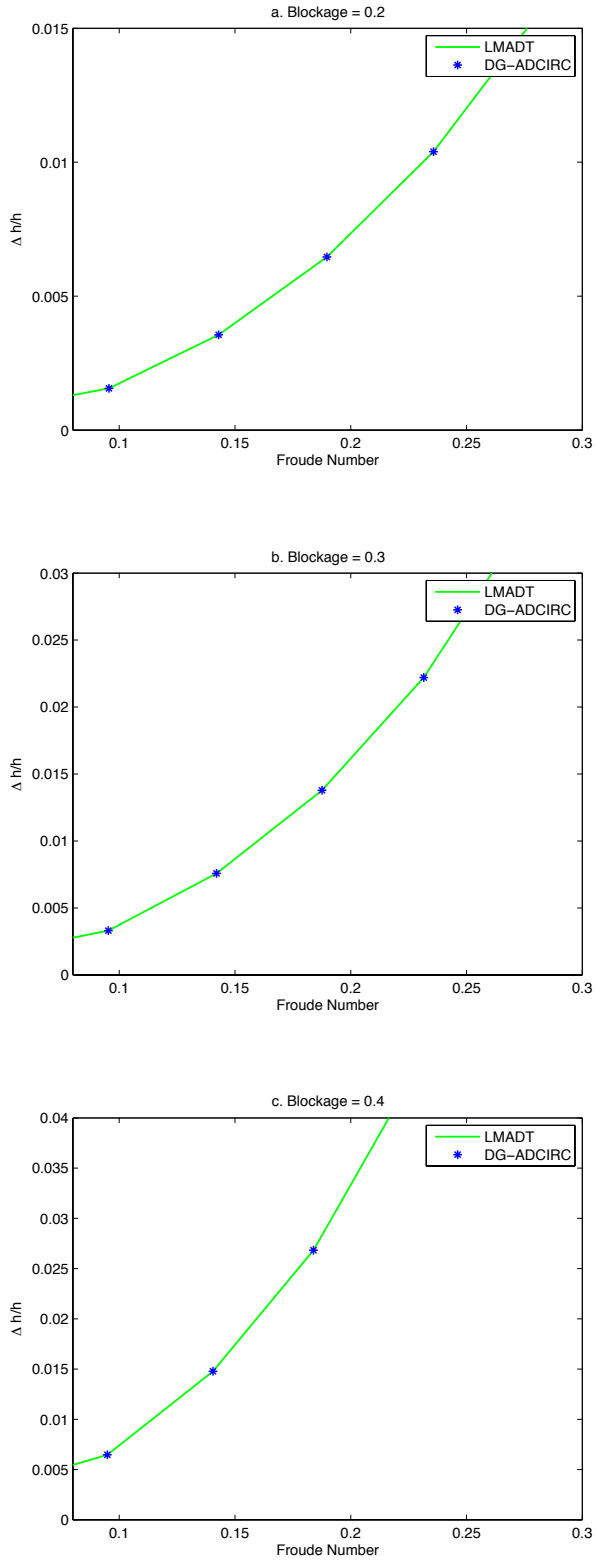

Figure 7 Comparisons against the analytical (LMADT) solution and numerical (DG-ADCIRC) solution for different upstream conditions. The results are plotted against different blockage ratios; a. Blockage = 0.2, b. Blockage = 0.3, c. Blockage = 0.4.

b. An idealised channel with partial blockage

In this example, different configurations of tidal fences that do not extend entirely across the channel are given. Figure 8 shows the unstructured triangular mesh, which is 4000 m in width and 10000 m in length. The coordinates are in latitude and longitude. The tidal fence is placed 2500 m away from the upstream forcing boundary (shown as a purple line in Figure 8). The water depth is set to 1.0 m, and the bed friction coefficient is $C_d = 5 \times 10^{-4}$ throughout the domain. In this example, bed friction has been added to the problem in order to achieve a steady solution and to avoid wake instabilities (following Draper, 2011). The upstream boundary is forced using a constant flow rate to achieve an upstream Froude number of approximately 0.1. A ramping duration of 0.5 days is implemented in order to prevent a shock wave in the solution. The downstream boundary is an elevation specified boundary, which is set to $H = 1.0$ m. Slip boundary conditions are applied at the sidewall boundaries. The turbine fence is characterized by a wake induction factor of $\alpha_4 = 1/3$ and a blockage ratio of $B = 0.6$. The effects of the momentum sink on free surface elevation and depth-averaged velocity field are shown in Figure 9 and Figure 10.

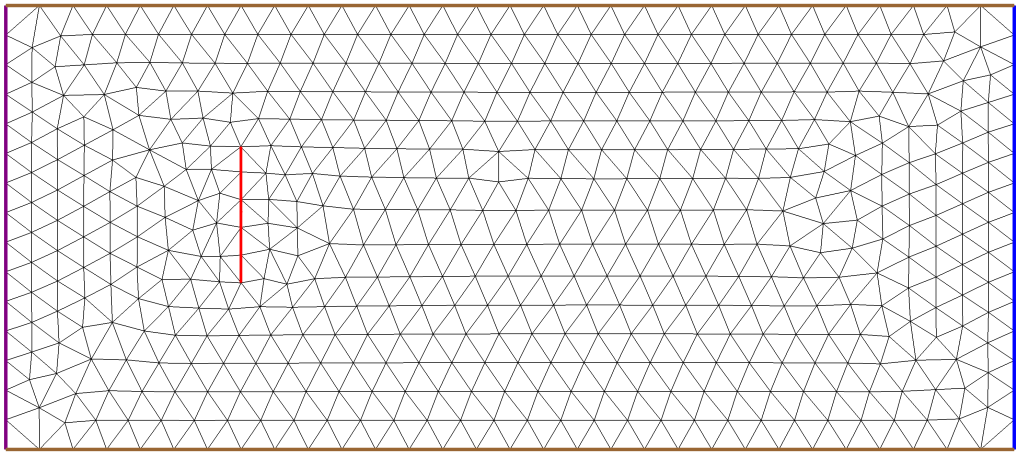

Figure 8 The unstructured triangular mesh used in the unbounded turbine configuration test case; the purple line shows the upstream boundary which is flux specified; blue line shows the downstream boundary which is held at a fix elevation of 1.0 m; red line demonstrates the location of turbine fence in the domain; and the brown lines show the sidewall boundaries.

A comparison of the computed and intended depth change along the fence is given in Table 2. DG-ADCIRC results are in good agreement with the intended relative depth change computed using LMADT. In the next subsection, the modified DG-ADCIRC code is tested against more complex problems.

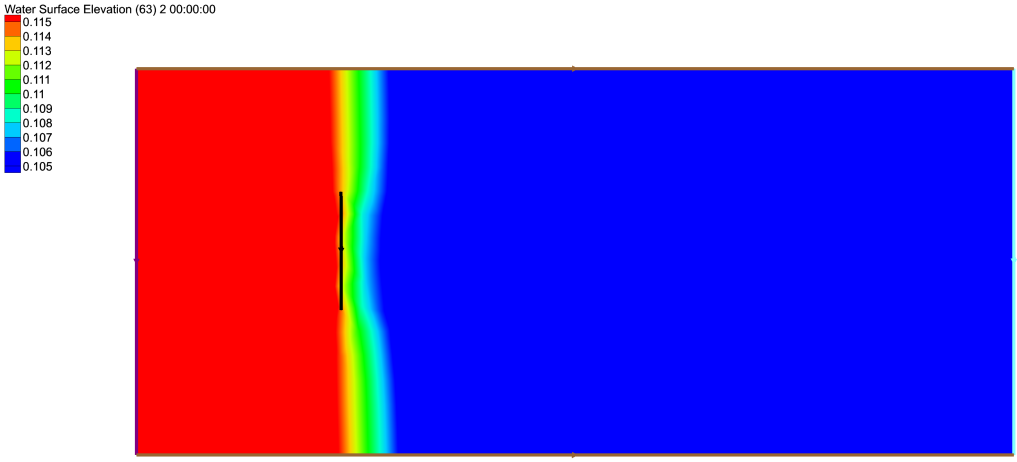

Figure 9 The effect of momentum sink on the free surface elevation profile. The brown line indicates the tidal fence configuration. The water surface elevations are in meters.

Position along the fence	**LMADT -** $\Delta H/H$	**DG-ADCIRC -** $\Delta H/H$
0	0	0
0.1	0.0075	0.0074
0.2	0.0076	0.0076
0.3	0.0079	0.0079
0.4	0.0079	0.0079
0.5	0.0081	0.0082
0.6	0.0079	0.0079
0.7	0.0079	0.0079
0.8	0.0076	0.0076
0.9	0.0075	0.0074
1	0	0

Table 2 Comparison of computed and intended relevant depth change along the tidal fence

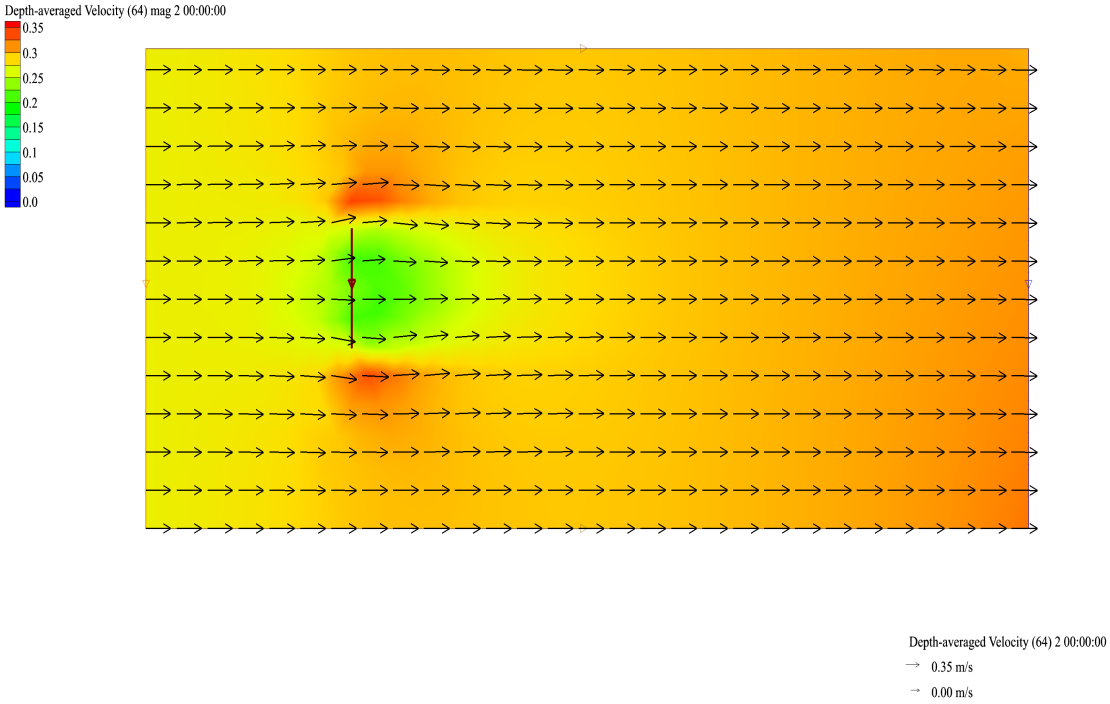

Figure 10 The effect of a momentum sink on the local velocity profile. The vectors indicate the magnitude and direction of the flow and are superimposed onto a regular grid. The depth-averaged velocity contours are in m/s.

c. Partially blocked channels with complex flow conditions

In this subsection, the modified DG-ADCIRC code has been tested for more complex problem settings. The first test considers an idealised channel, which is rotated by 30 degrees in the counter-clockwise direction. The purpose of this problem set up is to test the code's ability to cope with directionality in the flow domain. The total water depth is set to 1.0 m and the unbounded turbine fence is located in the first quarter of the channel, normal to the flow direction. The blockage ratio is set to 0.6 and the wake induction factor is 1/3. The boundary conditions are the same as the previous unbounded tidal fence test case. The coordinate system used is geographic (latitude and longitude). The resulting velocity field shown in Figure 11 is in very good agreement qualitatively with that in Figure 10 after rotation.

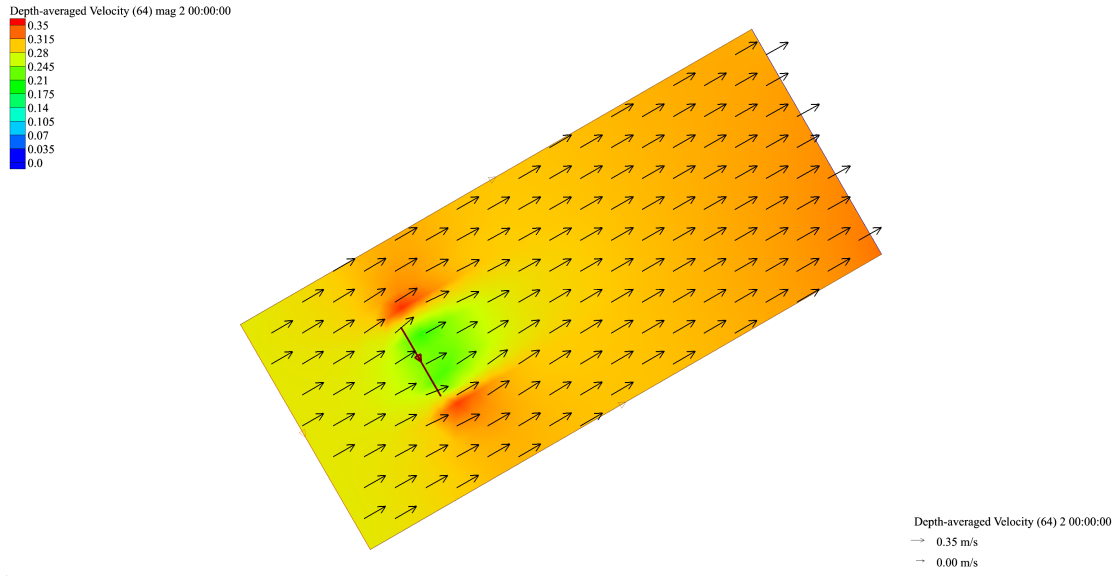

Figure 11 Rotated domain test case with unbounded tidal fence placed normal to the flow direction

WG3 WP6 aims to assess the availability of tidal energy resource around the selected sites using the modified DG-ADCIRC code that incorporates the LMADT algorithm. The numerical models created in the Milestone 2 (M2), are formed using the real bathymetric data, which indicates that the seabed changes arbitrarily within the computational domain. This test case therefore examines the capability of the modified DG-ADCIRC code to cope with non-uniform bathymetric conditions in the presence of tidal fences. Thus, the next test case considers the rotated idealised channel introduced previously, with variable bed topography. The change in the bathymetry is calculated with respect to the longitude of the nodes. The bathymetric depth is calculated as follows,

$$H_{variable} = 1 + \frac{longitude_{node}}{100} \qquad 4.13$$

Figure 12 shows the mesh used and the predicted velocity field. The results show higher velocities within the domain due to the decrease in the total water depth within the computational domain.

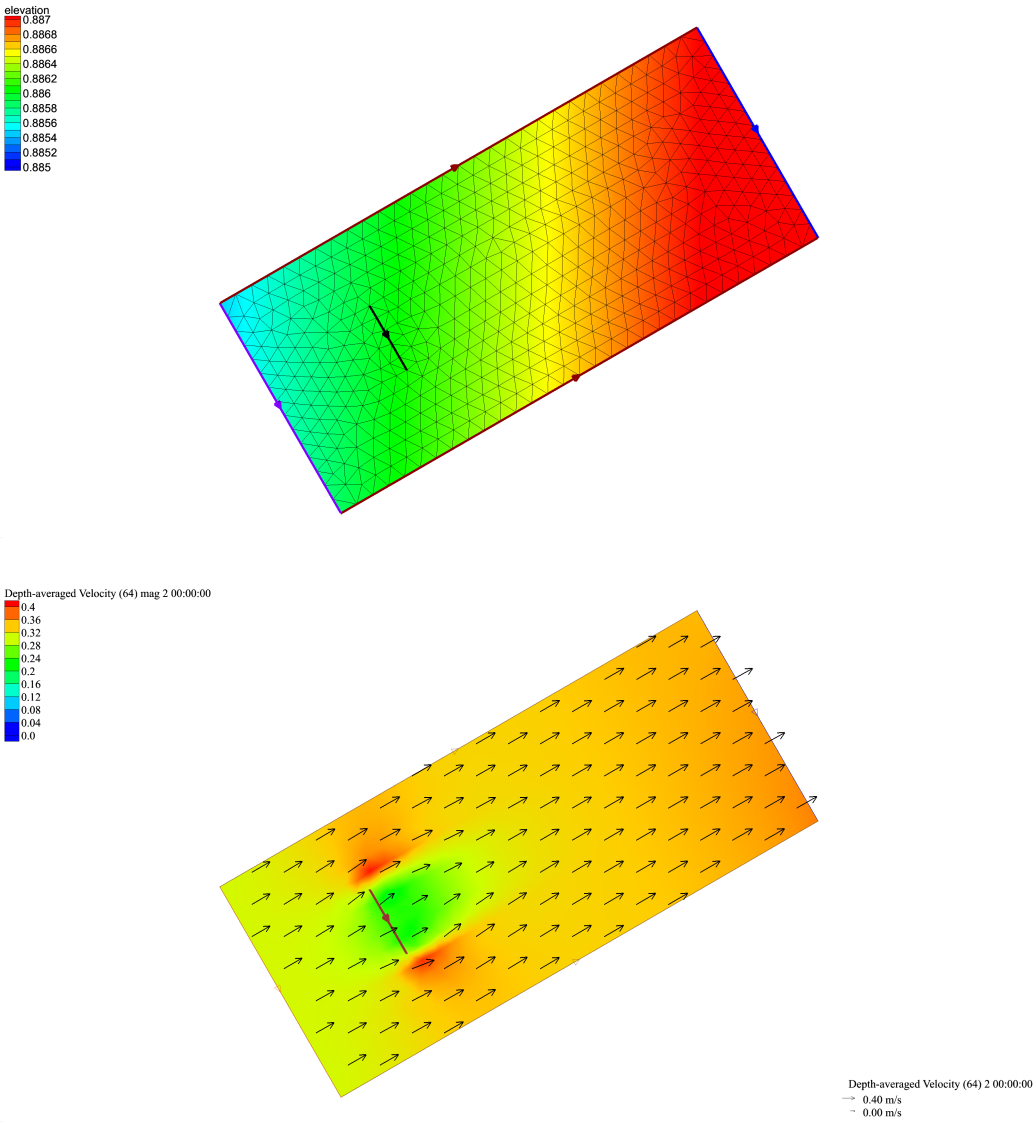

Figure 12 The computational mesh used in the problem showing the bathymetric depth within the domain (top), and the computed velocity field for a rotated rectangular channel with variable bathymetry (bottom). The contours are in metres.

The next test case examines the behaviour of the turbine model to non-normal flows. Figure 13 indicates the velocity field computed for an idealised horizontal channel, where the turbines are positioned at an angle of 60 degrees to the incoming flow.

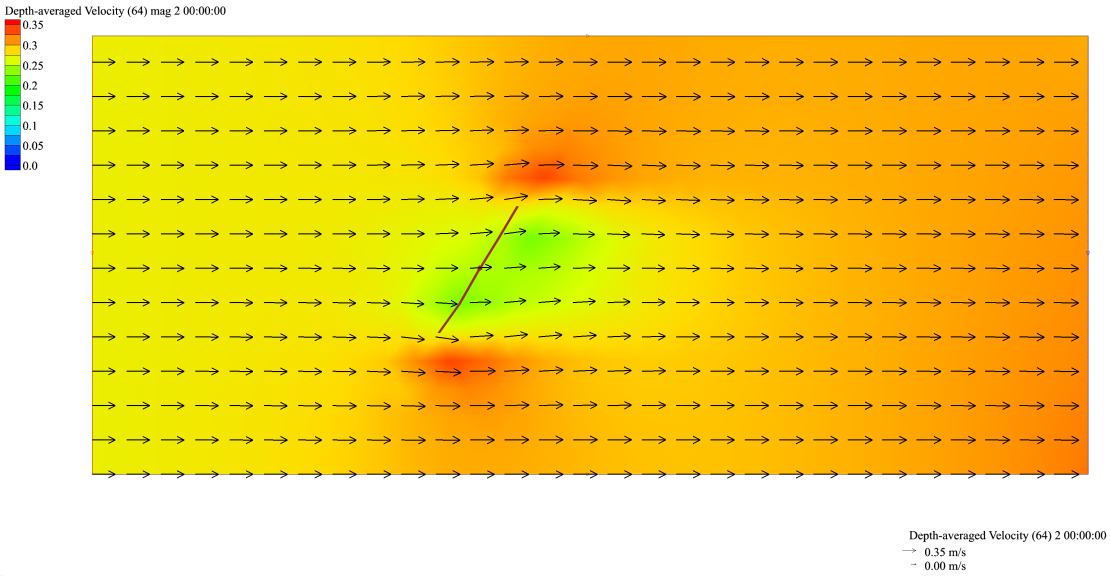

Figure 13 Idealised horizontal channel with unbounded turbines installed with an angle to the flow.

Lastly, a test case is created for an idealised horizontal channel with constant bed topography (1 m), where a rectangular island is located near to the upstream boundary. The unbounded tidal fence is inserted on the downstream of the island in order to test the capability of the modified code to cope with shed eddies. The computed velocities are shown in Figure 14. With this last test case, the modified DG-ADCIRC code, which uses the LMADT routine to represent the tidal turbines, proves to be stable when forced with realistic conditions.

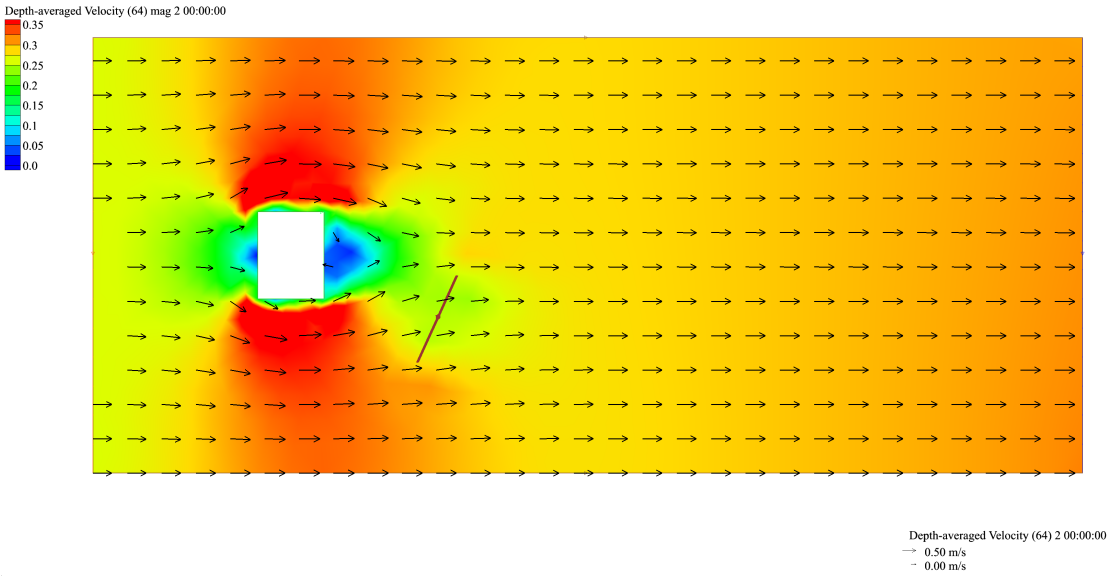

Figure 14 Idealised horizontal channel containing rectangular island. The turbine fence is indicated with the brown line on the downstream of the island.

5. Application of Line Sink of Momentum in 2D Depth-Averaged Shallow Water Models

This section presents the preliminary results for single array of turbines installed at the Anglesey Skerries. For the simulations, the modified DG-ADCIRC code is used which uses the line sink of momentum in order to represent FDC tidal arrays. The numerical model used in this section is an altered version of model presented in WG3 WP6 D4B, which includes the inter-tidal zones around the Bristol Channel. In the present model, the wetting and drying treatment is included in the computation. Table 3 outlines the model set up. In the model, first order piecewise linear elements are used. The numerical flux selected for the computations is the HLLC flux, introduced in Section 3. Second order, second stage Runge-Kutta time discretisation has been used in accordance with the linear elements used in the model.

Parameter	Value	Notes
Time-step	0.5 s	To ensure stability, the time-step must satisfy the CFL condition, and diffusivity criterion, and so is dependent on the finest mesh size and the polynomial order used.
Ramping duration	1 day	To avoid shock-waves developing in the computation
Simulation period	3 days	
Eddy viscosity coefficient	3 m^2/s	Average value adopted for basin-scale hydrodynamic models
Non-linear bed friction coefficient	0.0025	Average value for depth-averaged models
Coriolis Force	Varies	Derived from latitude and longitude
Harmonics used	M_2	Preliminary simulations forced with the most significant tidal harmonic constituent
Wetting and drying	On	In order to investigate the significance of using wetting and drying on regions such as the Severn Estuary on the numerical model

Table 3 Model set-up parameters

Tidal harmonic analysis has been undertaken to compare the model results with the observed M_2 amplitudes and phases in several stations (see Table 4). Very good agreement is obtained between predictions of the DG-ADCIRC model with the Admiralty Charts for an M_2 tidal constituent. Inclusion of the wetting and drying treatment has improved the model results in the Bristol Channel region, compared to the results presented in WG3 WP6 D4B.

Location	Observed (Admiralty Charts)		Predicted (DG-ADCIRC)	
	Amp., $H_n(m)$	Phase, $\varphi_n(^\circ)$	Amp., $H_n(m)$	Phase, $\varphi_n(^\circ)$
Heysham	3.19	325	3.21	328
Ramsey	2.42	328	2.45	324
Port of St. Mary	2.04	324	2.07	320
Port Dinorwic	1.70	301	1.72	298
Caernarfon	1.61	293	1.64	285
Moelfre	2.47	308	2.48	302
Amlwch	2.30	305	2.37	300
Cemaes Bay	2.13	307	2.22	301
Holyhead	1.81	292	1.88	287
St. Thomas	4.25	194	4.30	186
Minehead	3.59	183	3.56	173
Ilfracombe	3.04	162	3.01	162
Lundy	2.67	160	2.62	163
Port Isaac	2.47	144	2.42	151
Newquay	2.24	142	2.26	143
Milford Haven	2.22	173	2.19	176
Port Talbot	3.13	173	3.25	175
Barry	3.82	185	3.95	183

Table 4 Comparison of M_2 tidal amplitudes of phases around Scotland, England, the Isle of Man and Wales

A more detailed analysis for the influence of wetting and drying treatment in the present model will be given in WG3 WP6 D6. Although, an improvement in results is seen for the Bristol Channel observation stations, the model still under-predicts (~5%) the M_2 tidal amplitudes and predicts slightly different phases (by ~+3 degrees) for the Anglesey stations.

The present report aims to test the line sink of momentum method in order to represent the effects of FDC tidal arrays in two-dimensional depth-averaged models and to give an initial understanding about how the tidal turbines will affect the flow characteristics around the Anglesey Skerries.

The main Pentland Firth results will be discussed in WG3 WP6 D6 as the site is chosen for the cross-comparison with the EDF model, although some preliminary results using the enhanced bed friction model are reported in the present report as an Appendix (see Section 7).

Change in M_2 Tidal Constituent in the Anglesey Skerries

This section discusses the preliminary run results using the altered DG-ADCIRC code that accounts for a line sink of momentum for specified edges in the computational domain, applied in the Anglesey Skerries. Including line sink of momentum into the code requires several changes in the source code. WG3 WP6 D4B explains the specifications of the input files that DG-ADCIRC code requires. In order to assign turbine edges, which are naturally internal, the structure of the 'fort.14' file that defines the nodes, their coordinates, the triangulation of the nodes and boundary conditions has been modified. The modified DG-ADCIRC code, which incorporates LMADT algorithm, requires the user to define the nodes that are used to create the edges, which are representing the turbines in the computational domain, in the 'fort.14' file. After creating the turbine edges, the user needs to define the specification of the turbine diameter and the wake induction factor, which can be input in the 'fort.dg' file. In the algorithm, the turbine diameters are used rather than a fixed blockage ratio because of variations in the bathymetry. The blockage is then calculated from an equivalent turbine size within the computation locally. For axial

flow turbines with a specified turbine diameter, it is possible to calculate the spatial blockage ratio indicated as in Equation 5.1,

$$B_{local} = \frac{\pi D_{axial}^2}{4bH_{total}}. \qquad 5.1$$

where D_{axial} indicates the turbine diameter, b is the lateral spacing between axial flow turbines in the array and H_{total} is the total water depth. The computational mesh involves structured elements embedded within the unstructured mesh, in order to define the tidal arrays continuously within the domain. Figure 15 shows the structured elements embedded in the unstructured mesh in the vicinity of the Anglesey Skerries. The turbine array is indicated as a brown line located on the NE of the Skerries. The total length of the array is 7750 meters. The average water depth in the area, where the turbine array is located, is 50 m. The turbines are configured so that on average 15 m of the water-column is swept by the turbines. This gives a blockage ratio during the simulations between 0.23 – 0.38 depending on the bathymetry. In the simulations, same model set up is used as explained in Table 3.

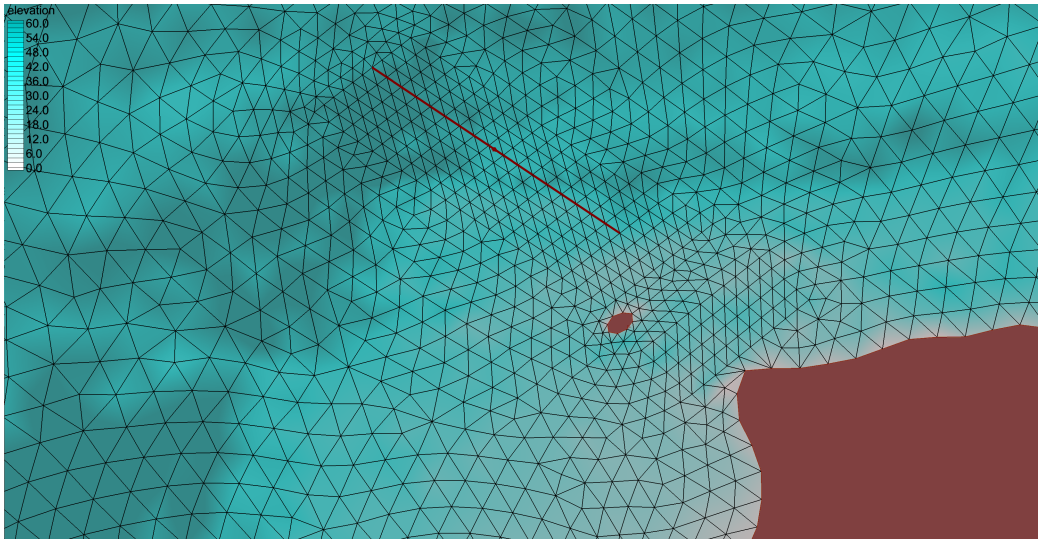

Figure 15 The structured elements embedded within the computational domain in the vicinity of the Anglesey Skerries

Two scenarios are considered for applying the DG-ADCIRC code within the Anglesey Skerries region. In the first case, the tidal devices are defined with a wake induction factor (α_4) of 0.9 and diameter of 22 m for an axial flow device. For this

test case, choosing α_4 as 0.9 gives a thrust coefficient on average of 0.28. Thus a mild change in the tidal regime is expected. For the next test case, the tidal turbine diameters are also set to be 22 m, but with a wake induction factor (α_4) of 0.4. Table 5 gives a similar comparison to Table 4, which lists the simulated M_2 amplitudes and phases within the simulations. Table 5 shows that in several observation stations close to the Anglesey Skerries, there are insignificant changes in the M_2 tidal amplitudes and phases.

Location	Base Case (No Turbine)		$D_{axial} = 22m; \alpha_4 = 0.9$		$D_{axial} = 22m; \alpha_4 = 0.4$	
	Amp., $H_n(m)$	Phase, $\varphi_n(^\circ)$	Amp., $H_n(m)$	Phase, $\varphi_n(^\circ)$	Amp., $H_n(m)$	Phase, $\varphi_n(^\circ)$
Port Dinorwic	1.72	298	1.72	298	1.73	299
Caernarfon	1.64	285	1.64	2.85	1.64	286
Moelfre	2.48	302	2.48	302	2.48	303
Amlwch	2.37	300	2.37	300	2.37	301
Cemaes Bay	2.22	301	2.23	301	2.25	302
Holyhead	1.88	287	1.89	288	1.89	288

Table 5 M_2 tidal amplitudes and phases predicted by the simulations for different cases

The impact of the turbine arrays can be seen in Figure 16 and Figure 17, which show the M_2 co-tidal amplitudes and phases respectively. Both figures include the base case where no turbines are included in the computation (the black line represents the location of turbines for cross-comparison), and the two turbine array cases using different wake induction factors. Figure 16 shows that the M_2 co-amplitude lines in the vicinity of the turbine array are changed due to the change in the velocity. The turbine array stands as an obstacle to the flow, which in turn slows down the flow passing through the turbine array. The increment in the M_2 co-tidal amplitude is shown in Figure 18. Figure 17 shows that in the vicinity of the turbines the high tide is observed in a shorter period than the natural case.

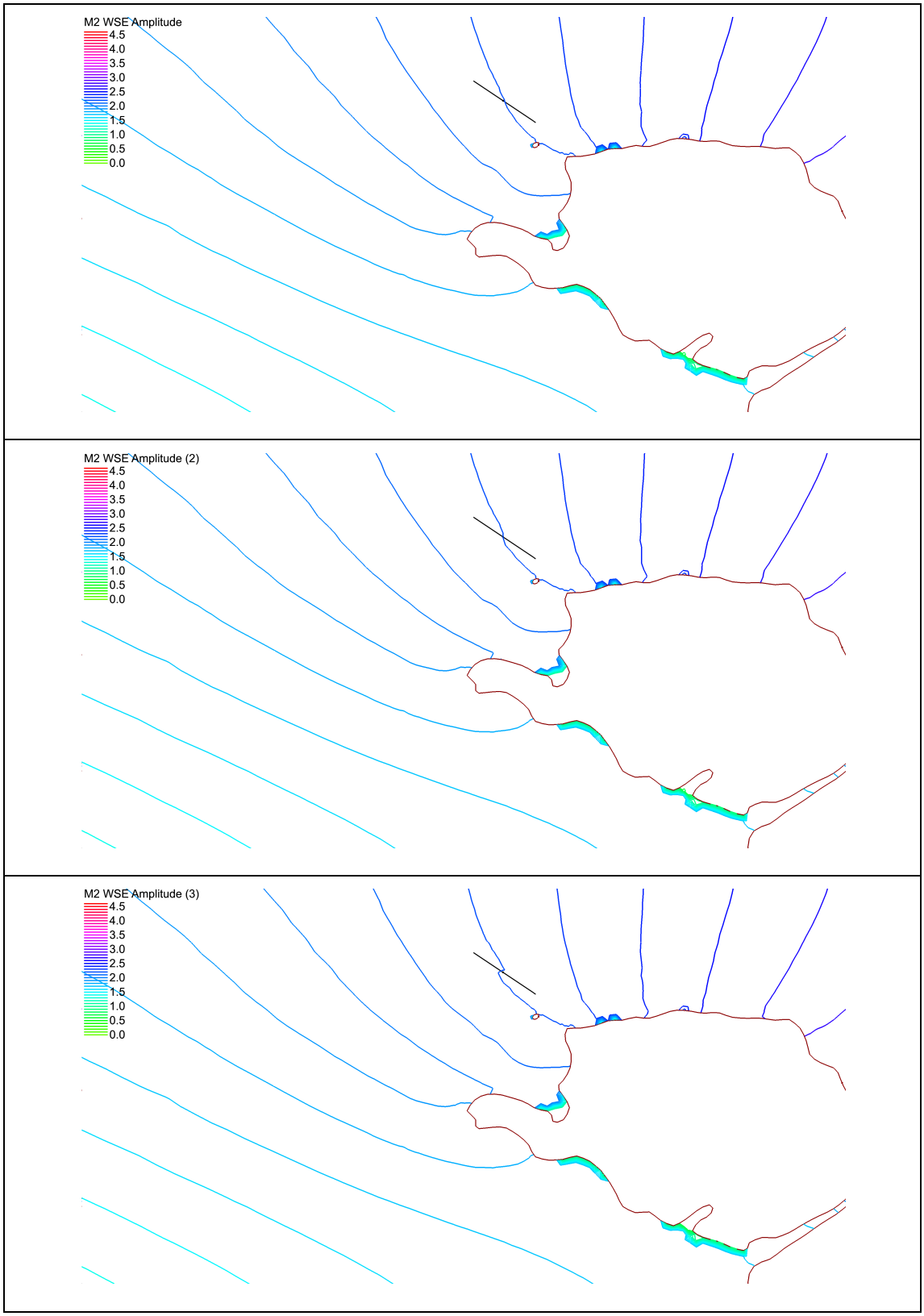

Figure 16 M_2 tidal amplitudes; (1) natural case, (2) al4 = 0.9, (3) al4 = 0.4. The axial tidal turbine diameter is 22.0 m and the blockage ratio is calculated with respect to the local water depths. The tidal turbine fence is indicated as a black line on the offshore of the Anglesey Skerries. The contour lines are in metres.

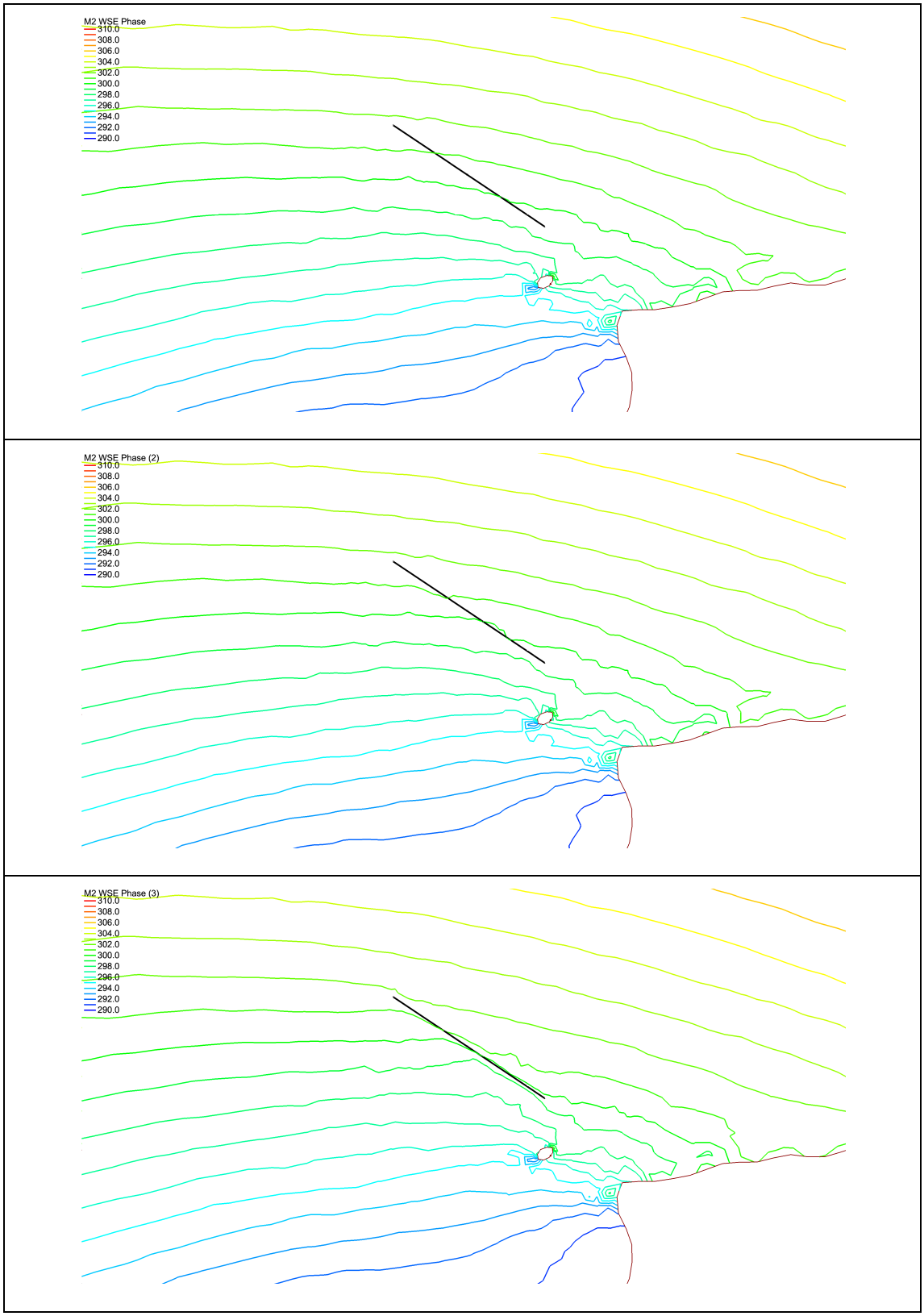

Figure 17 M_2 tidal phases; (1) natural case, (2) al4 = 0.9, (3) al4 = 0.4. The axial tidal turbine diameter is 22.0 m and the blockage ratio is calculated with respect to the local water depths. The tidal turbine fence is indicated as a black line on the offshore of the Anglesey Skerries. The contours are in degrees.

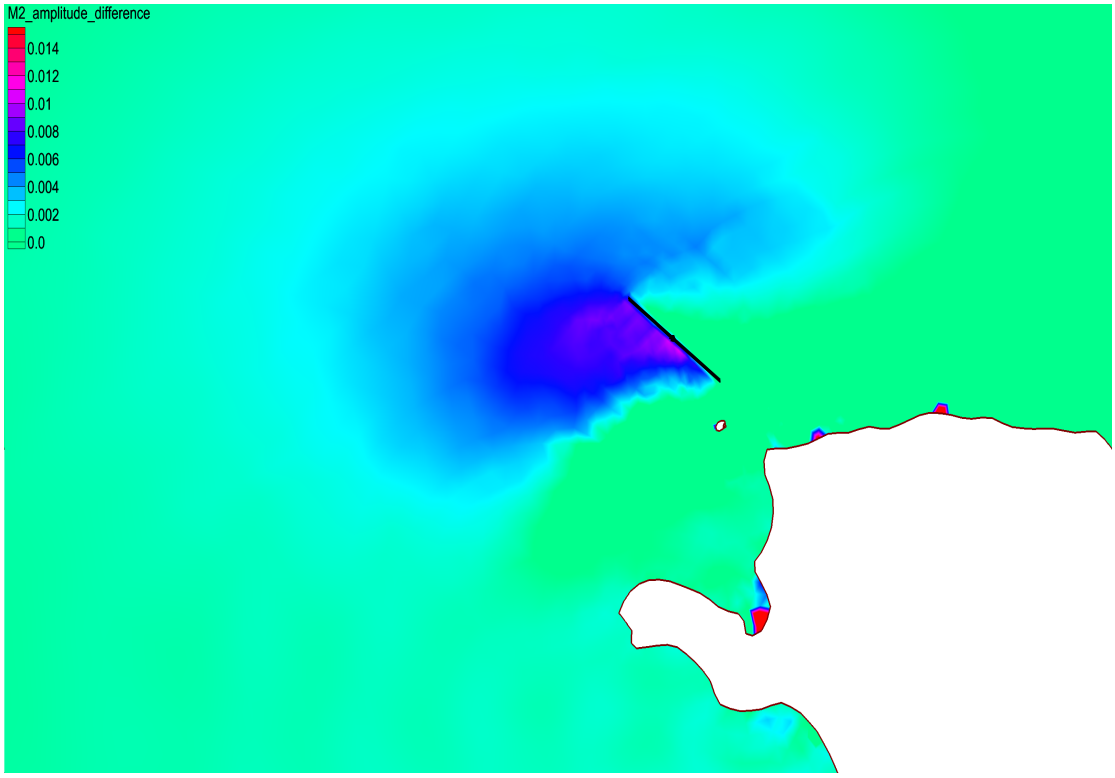

Figure 18 M_2 co-tidal amplitude change in the vicinity of the turbine array using turbines specified with diameter of 22.0 m and wake induction factor of 0.4. The contour plot is in metres.

Figure 19 shows the change in velocity magnitude seen in the area where turbine array is located. It is clear from the figure that, around the edges of the turbine array, the flow is accelerated. Along the fence, the flow is slowed down as the fence acts as an obstacle to the flow (shown as the green region in Figure 19). The largest reduction in velocity occurs in the region where the fastest flow occurs in the natural case (indicated as the dark blue contour in Figure 19). Figure 20 plots the change in velocity phases around the region where the tidal turbine fence is located. In the figure, it is seen that the maximum velocities are observed later than the natural case. The maximum velocity phase difference is approximately 10°, which indicates approximately a 30-min delay in the vicinity of the tidal turbine fence.

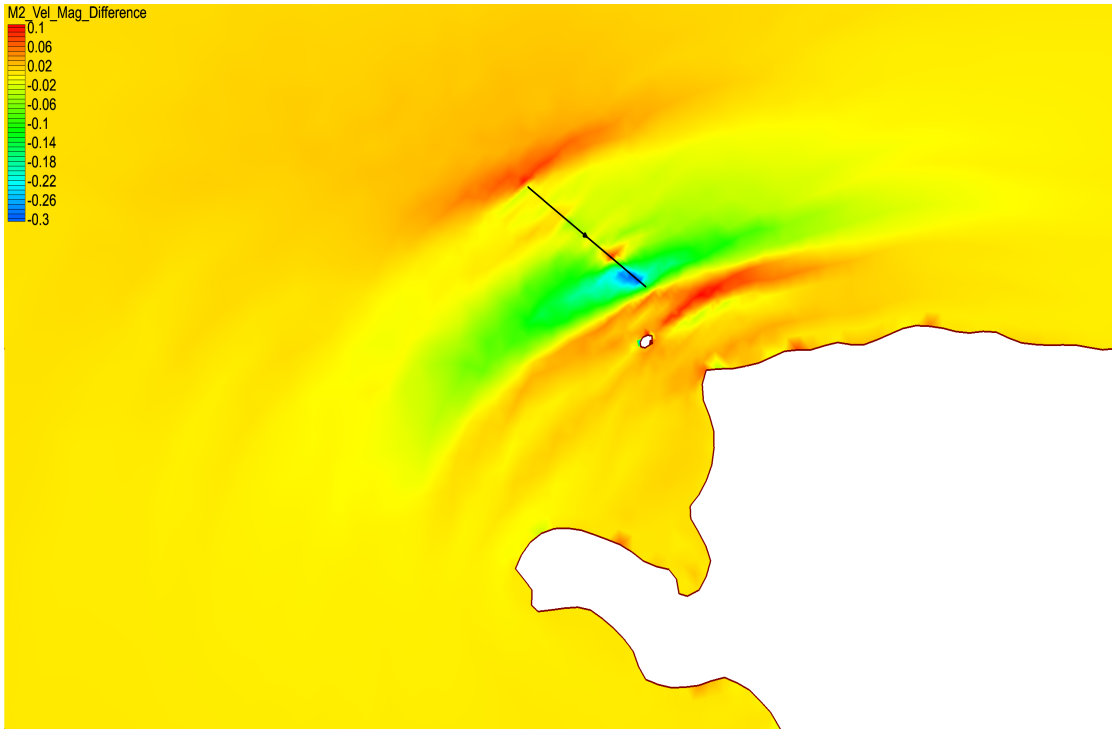

Figure 19 Change in velocity magnitude of M_2 tidal constituent in the vicinity of the tidal array. The contours are given in m/s.

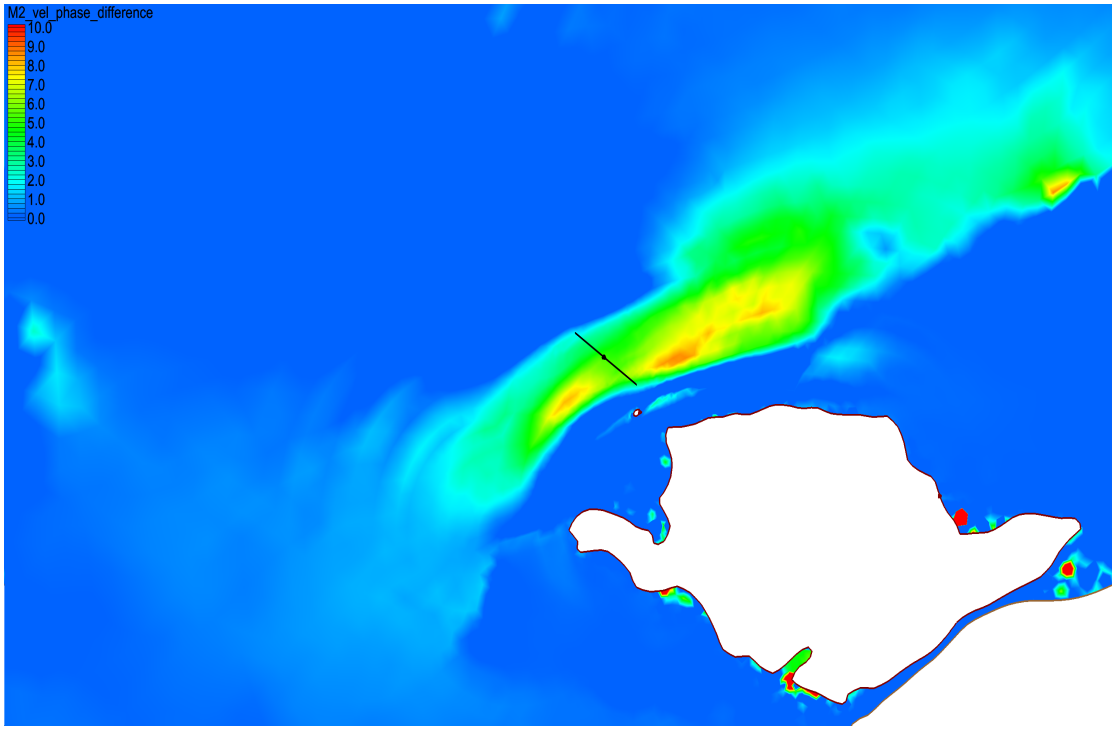

Figure 20 M_2 velocity phase difference in the vicinity of the turbine array. The contours indicate the phase change in degrees.

Power Generation

This section shows the preliminary results for average power extraction in the Anglesey Skerries. Using Equation 4.3 the power extracted from the flow can be calculated as,

$$P = \frac{1}{2}\rho u^3 Bbh\alpha_2\left(\beta_4^2 - \alpha_4^2\right) = \frac{1}{2}\rho u^3 BbhC_P. \qquad 5.2$$

In Equation 5.2, ρ is the fluid density, u is velocity of the flow, B is the blockage ratio dependent on the spatial water depths, b is the width of the analysis considered along the fence, h is the total water depth, β_4 is the bypass flow velocity coefficient, α_4 is the wake velocity coefficient, C_P is the power coefficient that equals to $C_P = \alpha_2 C_T = \alpha_2\left(\beta_4^2 - \alpha_4^2\right)$ and α_2 is the turbine flow velocity coefficient, which is given in Equation 4.1. Figure 21 shows the average power extracted by the turbine fence located in the Anglesey Skerries. The turbine diameters are taken as 22.0 m and the wake induction factor is 0.4.

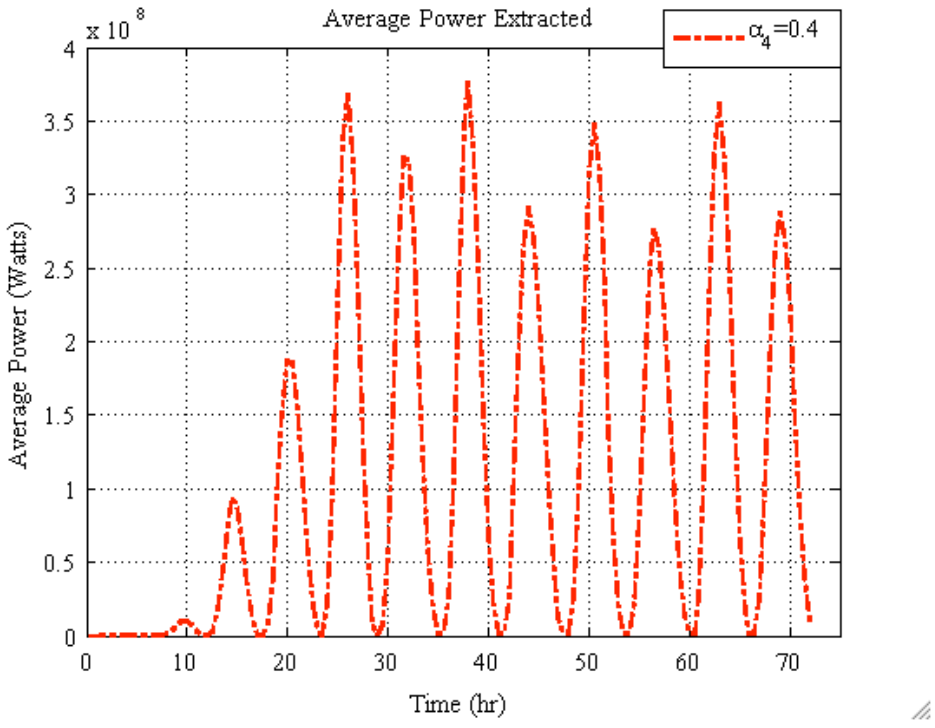

Figure 21 The power extracted in the Anglesey Skerries during the simulation. The axial tidal turbine diameter is 22.0 m and the wake induction factor is 0.4.

In the simulation, the tidal waves are ramped in gradually at the open boundaries during the spin-up period, thus in Figure 21 the average power extracted from the flow in the first few cycles is less than the rest of the simulation. The preliminary run gives ~350 MW (peak) extracted from the flow within a tidal cycle in the Anglesey Skerries by devices of the above specification. The average power extraction over the final 24 hours of the analysis is 140 MW. No attempt has yet been made to optimise the turbine properties or configuration. Note, very importantly, that the power extracted from the flow must not be confused with the actual power available for generation (see Houlsby *et al.*, 2008).

6. Conclusions

The present report gives a summary of the two-dimensional depth-averaged governing equations (SWEs) and the discontinuous Galerkin method, which is used to solve them. In WG3 WP6, a line sink of momentum method is used in the numerical model in order to incorporate the effects of tidal turbine fences in reality. The tidal fences are defined by using Linear Momentum Actuator Disc Theory and the code has been verified with different flow regimes. The modified DG-ADCIRC code is then used in the Anglesey Skerries region to test the algorithm. The results show that there is a change in the M_2 tides in the region where the turbine fence is located. The preliminary results given here are promising but further parametric studies need to be taken in order to predict the disturbance to the natural flow regime. These parametric studies are subjected to WG3 WP6 M4.

7. Appendix

The alternative approach to the line discontinuity was shown to work for idealised cases in WG3 WP6 D3. In this appendix results are presented showing how this has been applied to the model of the Pentland Firth developed in WG3 WP6 D4A. Note that more detail of these results will be presented in subsequent deliverables. Lines of enhanced roughness were considered across the channels of the Pentland Firth as shown in Figure 22.

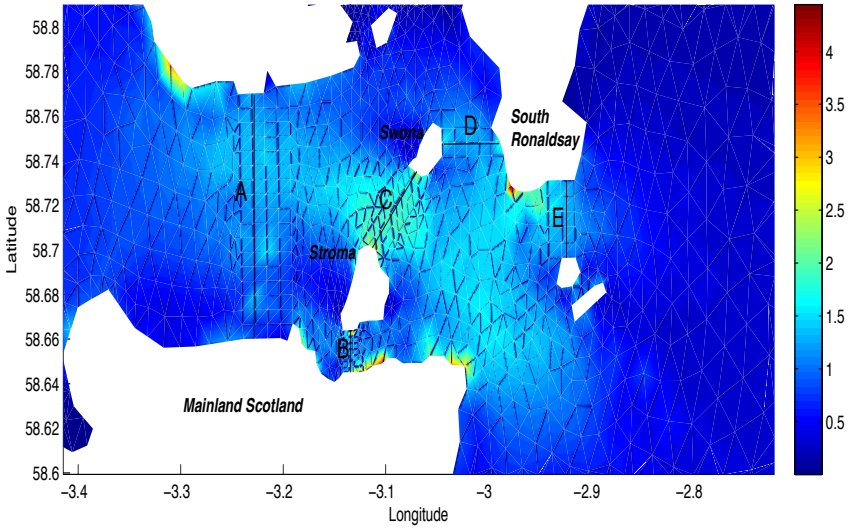

Figure 22 Locations of turbine fences within the numerical model. Colours show the rms velocity of the M_2 tidal components in m/s

First consider using enhanced roughness across the transect A (across the entire channel). As the thrust applied by the turbines is increased, the flow through the Pentland Firth reduces. Figure 23 shows how the power extracted from the flow, averaged over the tidal cycle, varies as a function of the maximum flow rate through the strait, Q_{nat}. The maximum average power which can be extracted is approximately 4 GW. This would require a reduction in the flow through the Pentland Firth to 55% of the natural value. However, it is possible to extract much of the power with a much smaller disturbance (e.g. 3 GW with only a 20% reduction in the maximum flow rate).

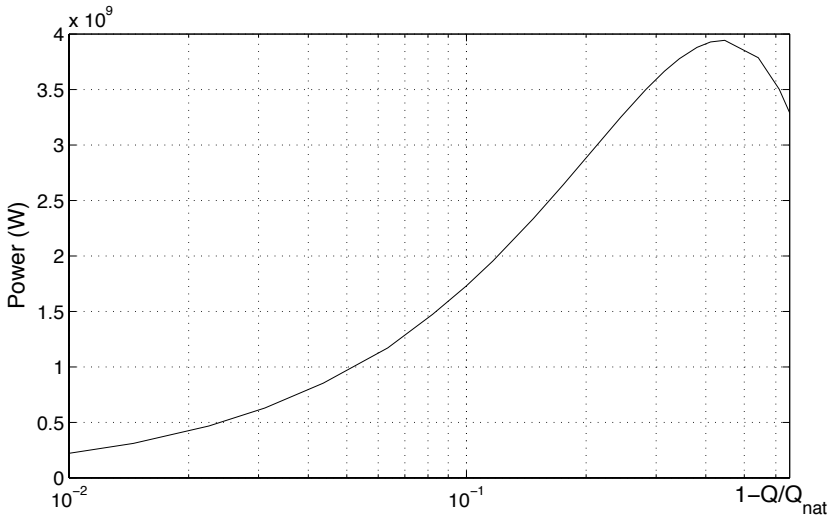

Figure 23 Average power extractable from the M_2 tide at transect A as a function of the flow rate.

In Figure 24 and Figure 25 the difference between the M_2 tidal dynamics for the case of maximum energy extraction are shown. The change in water level across the turbines can be clearly seen.

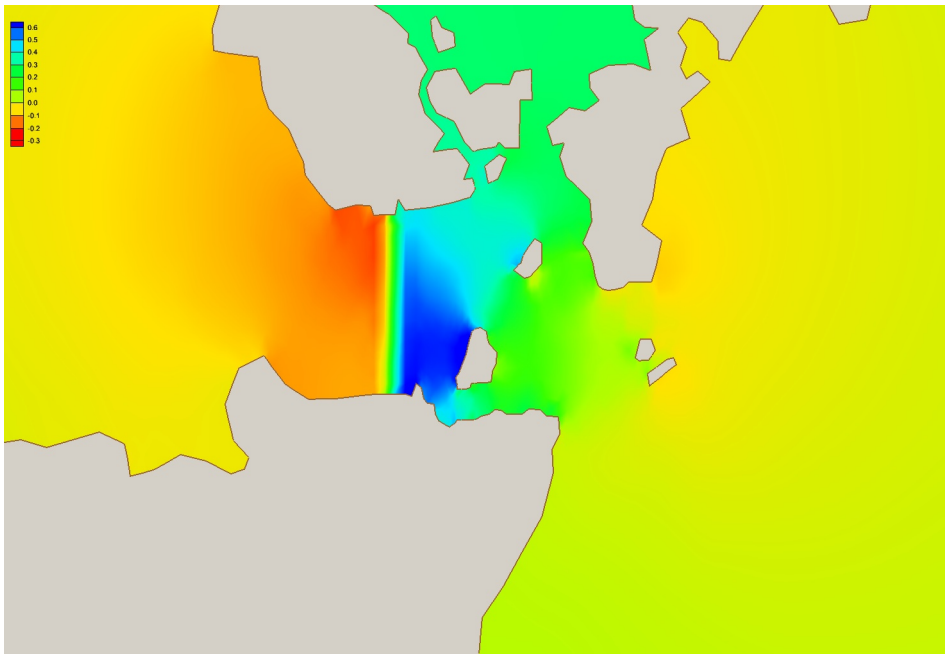

Figure 24 Change in M_2 water level between natural case and the point of maximum energy extraction for turbines at cross-section A. Water level in metres.

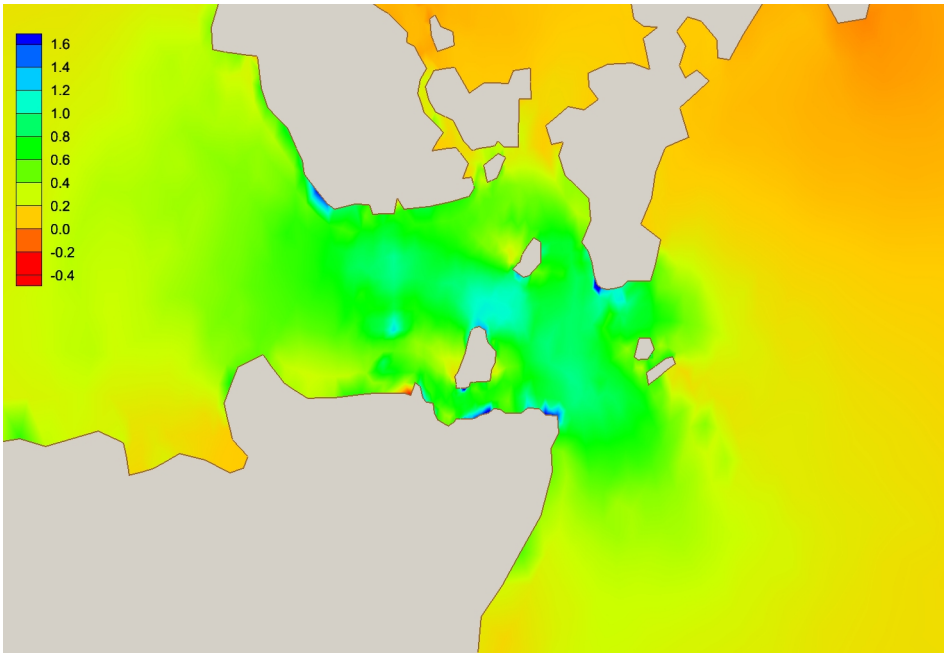

Figure 25 Change in M_2 current velocities between natural case and peak energy extraction for turbines at A. Velocities in m/s.

The peak energy predicted by the model is in good agreement with the simplified model of Garrett & Cummins (2005) providing additional verification of these results.

In Table 6, the peak power is presented, which may be extracted from the other sub-channels or from placing turbines across multiple channels. It can be seen that the resource of the sub-channels are interdependent. It can also be noted that power extracted along BCD combined is almost equivalent to 'A', suggesting that extracting the maximum resource is virtually independent of the location of the devices, if the entire flow through the Pentland Firth is intercepted.

These results are presented here for preliminary discussion, as much further work and analysis is required on these cases.

Maximum average power extracted (MW) for selected transect					Total average power (MW)
A	B	C	D	E	
3943					3943
	99				99
		1547			1547
			451		451
				240	240
	179	1611			1790
	121		466		587
	86			220	305
		1513		166	1622
		2401	1093		3494
				213	570
	248	2555	1136		3939

Table 6 Maximum extractable power, averaged over the tidal cycle, for the various transects of the Pentland Firth

REFERENCES

Abbott, M.B., and Minns, A.W., Computational Hydraulics, Ashgate Publishing Co., Brookfield, Ct. Great Britain, 1979.

Admiralty Tide Tables, Vol.1, United Kingdom and Ireland, Including European Channel Ports, 1997.

Betz, A., Das maximum der theoretisch möglichen ausnutzüng des windes durch windmotoren, Z. Gestamte Turbinenwesen, 26, 1920.

Blunden, L.S., and Bahaj, A.S., Tidal energy resource assessment for tidal stream generatirs, IMechE Part A: J. Power and Energy, Vol: 221, 2007, p:137-146.

Blain, C.A., and Massey, T.C., Application of a coupled discontinuous – continuous Galerkin finite element shallow water model to coastal ocean dynamics, Ocean Modelling 10, 2005, p: 283-315.

Bryden, I.G., Couch, S.J., Owen, A., and Melville, G., Tidal current resource assessment, Proc. IMech Vol. 221 Part A: J. Power and Energy, 2007, p: 125-135.

Cockburn, B., and Shu, C.W., Local discontinuous Galerkin method for time-dependant convection-diffusion systems, SIAM, Journal of Numerical Analysis, 35(6), 1998, p:2440-2463.

Draper, S., Tidal Stream Energy Extraction in Coastal Basins, DPhil Thesis, University of Oxford, 2011.

Dubiner, M., Spectral methods on triangles and other domains, J. Scientific Comput. 6, 1998, p: 357-372.

Falconer, R. A., An introduction to nearly horizontal flows in Coastal, Estuarial and Harbour Engineers' Reference Book, 1993 (Abbott, M. B. & Price, W. A., eds). E & FNSpon Ltd., London, pp.736

Ferrer, E., A high order discontinuous Galerkin - Fourier incompressible 3D Navier-Stokes solver with rotating sliding meshes for simulating cross-flow turbines, DPhil Thesis, University of Oxford, 2012.

Froude, R.E., Transactions, Institute of Naval Architects, 30:390, 1889.

Garcia-Navarro, P., Brufau, P., Burguete, J., and Murillo, J., The shallow water equations: An example of hyperbolic system, Monografias de la Real Acadeia de Ciencias de Zaragoza, 2008, Vol. 31, pp.89-119.

Houlsby, G.T., Draper, S., and Oldfield, M.L.G., Application of Linear Momentum Actuator Disc Theory to Open Channel Flow, Technical Report, Department of Engineering Science, University of Oxford, January 2008.

Houston, P., Senior, B., and Suli, E., hp-Discontinuous Galerkin finite element methods for hyperbolic problems: error analysis and adaptivity, International Journal for Numerical Methods in Fluids, 2002, 40:153-169.

Karniadakis, G. E., and Sherwin, S., Spectral/hp Element Methods for Computational Fluid Dynamics, 2nd Edition, Oxford Science Publications, p: 310-548, 2005.

Kubatko, E.J., Westerink, J.J., and Dawson, C., An unstructured grid morphodynamic model with a discontinuous Galerkin method for bed evolution, Ocean Modelling Vol: 15, 2006, p: 71-89.

Lanchester, F.W., A contribution to the theory of propulsion and the screw propeller, Trans. Inst. Naval Archit., LVII:98 116, 1915.

Shu, C.W., and Osher, S., Efficient implementation of essentially non-oscillatory shock-capturing schemes, J. Computational Physics, Vol.77, 1988, p: 439-471.

Sutherland, G., Foreman, M., and Garrett, C., Tidal current energy assessment for Johnstone Strait, Vancouver Island, Proc. IMechE Vol. 221, Part A: J. Power and Energy, 2007, p: 147-157.

Tassi, P.A., Bokhove, O., and Vionnet, C.A., Space discontinuous Galerkin method for shallow water flows- kinetic and HLLC flux, and potential vorticity generation, Advances in Water Resources, 2007, 30:998-1015.

Toro, E. F., Shock-capturing methods for free-surface shallow flows, Wiley, New York, 2001.

Van Kuik, G.A.M., The Lancester-Betz-Joukowsky Limit, Wind Energy, Vol.10, 2007, p.289-291.

Vreugdenhil, C.B., Numerical methods for shallow-water flow, 1994, Kluwer Academic Publishers, Water Science and Technology Library, The Netherlands.

Wei Yan, T., Shallow water hydrodynamics, 1992, Elsevier Oceanography Series, Water&Power Press, Beijing.